

Time and length scales of ice morphodynamics driven by subsurface shear turbulence

Diego Perissutti^{1,2} , Cristian Marchioli² and Alfredo Soldati^{1,2}

¹Institute of Fluid Mechanics and Heat Transfer, TU-Wien, 1060 Vienna, Austria

²Polytechnic Department of Engineering and Architecture, University of Udine, 33100 Udine, Italy

Corresponding author: Alfredo Soldati, alfredo.soldati@tuwien.ac.at

(Received 27 March 2025; revised 13 June 2025; accepted 27 July 2025)

The interaction between deep oceanic currents and an ice base is critical to accurately predict global ice melting rates, yet predictions are often affected by inaccuracies due to inadequate dynamical modelling of the ice–water interface morphology. To improve current predictive models, we numerically investigate the evolution of the ice–water interface under a subsurface turbulent shear-dominated flow, focusing on the time and length scales that govern both global and local morphological features. Based on our previous work (Perissutti, Marchioli & Soldati 2024 *Intl J. Multiphase Flow* **181**, 105007), where we confirmed the existence of a threshold Reynolds number below which only streamwise-oriented topography forms and above which a larger-scale spanwise topography emerges and coexists with the streamwise structures, we explore three orders of magnitude for the Stefan number (the ratio of sensible heat to latent heat). We examine its impact on ice melting and its role in shaping the interface across the two distinct morphodynamic regimes. We identify characteristic time scales of ice melting and demonstrate that the key features of ice morphodynamics scale consistently with the Stefan number and the Péclet number (the ratio of heat advection to diffusion) in both regimes. These scaling relationships can be leveraged to infer the main morphodynamic characteristics of the ice–water interface from direct numerical simulation datasets generated at computationally feasible values of Péclet and Stefan numbers, enabling the incorporation of morphodynamics into geophysical melting models and thereby enhancing their predictive accuracy.

Key words: solidification/melting, turbulence simulation, multiphase flow

1. Introduction

The basal melting of ice plays a critical role in the regulation of oceanic currents (Ezat, Fahl & Rasmussen 2024), sea level (Pritchard *et al.* 2012), water temperature (Clark, Alley & Pollard 1999) and therefore broader climate dynamics (Alley *et al.* 2005; Golledge *et al.* 2019). In fact, basal melting is one of the main contributors to global mass loss of ice shelves in the ocean, accounting for as much of a loss as calving (Rignot *et al.* 2013). The melting process is significantly modulated by the interaction between the warm deep-water currents and the ice base, which also shapes the morphology of the ice–water interface. This effect, in turn, influences the global distribution of heat and salinity, thus driving oceanic circulation patterns. The morphological patterns produced by melting, e.g. on ice shelves (Hobson, Sherman & McGill 2011; Lucieer *et al.* 2016; Hirano 2023; Washam 2023), result from a combination of heat and mass transfer processes, but also depend on the speed of the water flow beneath the ice (Ashton & Kennedy 1972; Gilpin, Hirata & Cheng 1980; Bushuk *et al.* 2019), which is most often turbulent (Davis & Nicholls 2019). When the water velocity exceeds a certain threshold, specific features appear on the ice interface, creating feedback effects that can influence the hydrodynamic roughness (Jia, Andreotti & Claudin 2023), overall melt rates (Gilpin *et al.* 1980; Wettlaufer 1991; Feltham, Worster & Wettlaufer 2002) and, in turn, the stability of ice sheets (Joughin & Alley 2011; Alley *et al.* 2016). A detailed understanding of these dynamics is thus crucial to quantify global melt rates and refine the predictions of climate models (Patmore *et al.* 2023).

The dynamics of ice–water interfaces has been widely explored in the literature, primarily in buoyancy-driven flows (Rabbanipour *et al.* 2018; Wang *et al.* 2021*a,b,c*; Yang *et al.* 2022; Dhas, Roy & Toppaladoddi 2023; Du *et al.* 2023; Yang *et al.* 2023*a*; Fang *et al.* 2024), but also in interplanetary environments (Gastine & Favier 2024) or in porous media (Magnani *et al.* 2024). However, a complete explanation of the physical mechanisms that control the interface evolution remains elusive, especially under strong shear conditions (Bushuk *et al.* 2019). In fact, most of the numerical studies that analyse the interactions with a shearing flow, consider laminar conditions (Camporeale & Ridolfi 2012; Toppaladoddi & Wettlaufer 2019; Hester *et al.* 2021; Yang *et al.* 2024), with very few exceptions in the turbulent regime (Couston *et al.* 2021; Perissutti *et al.* 2024). The need for further studies is driven by the fact that almost all current ice melting models make use of empirical correlations or simplified heat transfer estimates that are based on the assumption of a flat, isothermal interface. This is often the case for models of basal melting in icebergs (FitzMaurice *et al.* 2016; Cenedese & Straneo 2023) and ice shelves (Dinniman *et al.* 2016; Goldberg *et al.* 2019). However, such models can produce errors in melt rate predictions of up to an order of magnitude (Yoshihiro *et al.* 2019; Jourdain *et al.* 2020), and are often unable to capture the high variability observed in experimental data (Bushuk *et al.* 2019). Incorporating morphodynamic effects on local heat and mass transfer is therefore essential to improve model accuracy, the key challenge being how to integrate these factors into existing parameterizations (Hewitt 2020; Du, Calzavarini & Sun 2024; Toppaladoddi & Wells 2025).

The morphology of an ice–water interface subject to strong shear can be very complex. Foundational studies by Ashton & Kennedy (1972) and Hsu, Locher & Kennedy (1979) documented the formation of unstable spanwise wavy patterns (referred to as ripples hereinafter) at the interface, a phenomenon later confirmed by laboratory experiments (Gilpin *et al.* 1980; Ramudu *et al.* 2016; Bushuk *et al.* 2019). These patterns are quite common in many other contexts where an ablative surface interacts with a shearing flow (Claudin, Duràn & Andreotti 2017). Examples include sand beds (Khosronejad &

Sotiropoulos 2017; Duran Vinent *et al.* 2019; Yizhaq 2024), limestone caves eroded by water (Curl 1974; Thomas 1979), air–ice interfaces (Bintanja, Reijmer & Hulscher 2001) or even meteorites (Lin & Qun 1987). Ripples emerge when the shear Reynolds number of the flow surpasses a critical threshold, defining the conditions by which the interaction between ice streamwise advection and cross-stream diffusion of heat and momentum results in the spontaneous formation of these ice structures.

Most of the studies that have documented the formation and dynamical evolution of ice ripples are theoretical and/or experimental (Ashton & Kennedy 1972; Gilpin *et al.* 1980; Camporeale & Ridolfi 2012; Bushuk *et al.* 2019). Only recently, the direct numerical simulation (DNS) of turbulence, coupled with heat transfer and a phase-changing interface, has been applied to the study of ice melting: specifically, Couston *et al.* (2021) studied the shear-driven evolving topography of an ice layer. They reported the formation and evolution of streamwise-oriented ice structures. Possibly due to the low Reynolds number examined, they observed no spanwise-oriented ice topography (Couston *et al.* 2021). Following Couston *et al.* (2021), in a previous work (Perissutti *et al.* 2024) we performed a series of DNS to investigate the morphodynamics of an ice layer melting and freezing over a turbulent stream of warm water, and we examined the ice morphodynamics at a Reynolds number similar to that investigated by Couston *et al.* (2021) and at one significantly higher. At the lower Reynolds number, streamwise-oriented, streaky ice structures of much smaller length scale are formed, in agreement with the findings of Couston (2021). At the higher Reynolds number, spanwise morphology evolves exhibiting ripples of greater length scale that coexist with the streaky ice structures. These findings confirm the existence of a certain minimum Reynolds number necessary to observe these structures, and further establish that DNS is an accurate method for the study ice melting in flowing fluids because it allows all the relevant thermofluid dynamic processes to be directly implemented. The main limitation of this approach is the high computational cost, which prevents its applicability to the large separations in time and length scales that characterize actual environmental melting processes. In practical cases, the large-scale fluid circulation is much slower than the smallest turbulence scales, and similarly, the time scale of latent heat transfer is much larger than that of sensible heat transfer. As a result, both the Reynolds number, which represents the ratio between the flow advection and viscous time scales, and the Stefan number (St), which represents the ratio between the time scales of latent heat transfer and sensible heat transfer, tend to be very large. Additionally, the melting process is characterized by the Péclet number (Pe), which describes the relationship between the time scales of advection and heat diffusion. Simulating realistic values for these three numbers – Reynolds, Stefan and Péclet – is the biggest challenge when performing DNS of shear-driven melting. In fact, all previous studies based on DNS (Couston 2021; Yang *et al.* 2023b; Perissutti *et al.* 2024) considered Stefan numbers close to unity or smaller, these values being approximately two orders of magnitude lower than those typical of shear-driven melting. Since the Stefan number quantifies the time scale separation between melting and heat diffusion, simulating a lower St reduces computational costs by fictitiously accelerating the melting process relative to heat diffusion.

In the present work, we aim to address the effect of such time scale separation by investigating a broader range of parameters that cover two orders of magnitude for the Stefan number (up to a value $St = 10$) and better describes real-case scenarios. The simulated values of the Stefan number were chosen by exploiting the analytical solution of the Stefan problem (discussed in § 2) as a compass for the simulations. This allowed us to infer with precision the time scales of the melting process under investigation and,

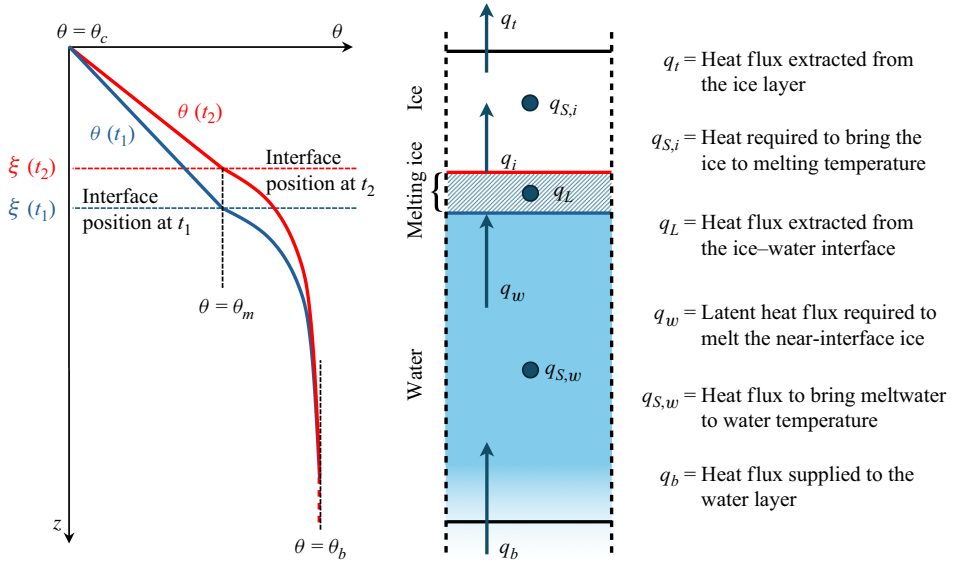


Figure 1. Schematic representation of the physical problem and heat flux balance. We consider an ice layer of thickness ξ on top of a layer of flowing water that is heated from below. The heat flux supplied to the water layer, q_b , is partly converted into sensible heat flux, $q_{S,w}$, which brings the meltwater to the same local temperature of the water stream. The heat flux q_w is then supplied to the ice–water interface, where it is partly converted into latent heat of fusion, q_L , which is responsible for the melting of the interface. The heat flux q_i is then extracted from the interface and partly converted into sensible heat, $q_{S,i}$, which brings the ice to melting temperature. Finally, the heat flux q_t is extracted from the system through the top of the ice layer. Due to melting, the thickness ξ reduces over time such that, given two generic time instants t_1 and $t_2 > t_1$, $\xi(t_1) < \xi(t_2)$. At steady-state, $q_b = q_t$ because all other sensible and latent heat contributions vanish.

in turn, the range of computational feasibility for the Stefan number by estimating the cost of the simulations at high St . We also varied the Reynolds number (and consequently the Péclet number), considering the same values as in Perissutti *et al.* (2024): one below the critical threshold for ripple formation and one well above it. In this paper, we analyse the morphodynamics of the ice–water interface in these two cases (§ 4), focusing first on the effect of the Stefan number. We then assess how the different morphological features of the interface scale with St and Pe . In particular, we investigate in detail the complex dynamics of the ice ripples that form at the largest Reynolds number, providing scaling relations that describe their evolution at varying St and Pe . These scaling relations can be used to predict the main features of the interface morphodynamics and the characteristic time scales of the melting process at Stefan and Péclet numbers that cannot be tackled using DNS.

2. The Stefan problem for ice melting

In this section, we introduce a simple one-dimensional (1-D) analytical model that can be used to estimate the time scales of melting of an ice layer heated from below by a turbulent stream of warm water. A schematic representation of the problem is provided in figure 1. The ice layer is subjected to a constant heat flux from below with an imposed temperature at the top. As melting takes place, heat is exchanged through the water layer and the ice layer. The heat flux, q_b , coming from the bulk of the water stream (or, equivalently, from the bottom boundary of the computational domain) is partly converted into sensible heat, $q_{S,w}$, which is needed to bring the temperature of the meltwater (namely, the water that

forms as a result of ice melting) to the local water temperature. The heat flux $q_w = q_b - q_{S,w}$ is exchanged through the ice–water interface and is partly converted into latent heat, q_L , during melting. The effective heat flux supplied to the ice layer, $q_i = q_w - q_L$, is then partly converted into sensible heat, $q_{S,i}$, which is required to bring the ice to melting temperature. As a result of such flux balance, the heat flux $q_t = q_i - q_{S,i}$ may be extracted from the ice layer and leaves the domain through its top boundary. Note that, at steady-state, the latent and sensible heat fluxes q_L , $q_{S,i}$ and $q_{S,w}$ are zero, yielding the equilibrium condition $q_b = q_t$.

To derive the model, in § 2.1, we first consider the heat transfer balance within the ice layer alone, described as a 1-D one-phase Stefan problem in which the standard Stefan condition has been modified to account for the effect of q_w on the time evolution of the ice thickness. We then solve this modified Stefan problem in the limit of high Stefan numbers: in this limit, an analytical solution for the ice thickness can be obtained and a closed formula for the time required to reach the equilibrium condition can be derived. In § 2.2, we extend the model to incorporate the effect of the heat transfer within the water layer, where q_b represents the heat forcing input.

2.1. The one-phase Stefan problem

We consider a 1-D Stefan problem in which an ice layer of thickness ξ is subjected to an arbitrary constant thermal forcing, q_w , at the bottom boundary (corresponding to the moving ice–water interface) and an imposed temperature on the top boundary. The ice layer extends from $z = 0$ to $z = \xi(t)$, which represents the instantaneous position of the ice–water interface. Any point where $z > \xi(t)$ falls inside the water layer. The temperature, $\theta = \theta(z, t)$, is set equal to a constant value below the freezing point, $\theta_c < 0$, at $z = 0$ and to the melting temperature, $\theta_m = 0$, at $z = \xi(t)$. Moreover, q_w is defined such that it is positive when transferred from ice to water: hence, q_w is always negative during melting. The dimensionless governing equations (see [Appendix A](#) for details on their non-dimensionalization) read as

$$\begin{cases} Pe \, St \frac{d\xi}{dt} = \left. \frac{\partial \theta}{\partial z} \right|_{z=\xi} + q_w, \\ \frac{\partial \theta}{\partial t} = \frac{1}{Pe} \frac{\partial^2 \theta}{\partial z^2}, \end{cases} \quad (2.1)$$

with the following boundary conditions

$$\theta(z = 0, t) = \theta_c, \quad (2.2)$$

$$\theta(z = \xi(t), t) = 0, \quad (2.3)$$

$$\theta(z, t = 0) = \theta_c(1 - z/\xi_0), \quad (2.4)$$

$$\xi(0) = \xi_0. \quad (2.5)$$

The dimensionless groups in (2.1) are defined as follows

$$St = \frac{\tilde{\mathcal{L}}}{\tilde{c}_p \Delta \tilde{\theta}}, \quad Pe = \frac{\tilde{\rho} \tilde{c}_p \tilde{u}_{ref} \tilde{h}_{ref}}{\tilde{\lambda}}; \quad (2.6)$$

where the notation $\tilde{\bullet}$ indicates that the quantity \bullet is dimensional; $\tilde{\mathcal{L}}$ is the specific latent heat, $\tilde{\rho}$ the density, \tilde{c}_p the specific heat at constant pressure, $\tilde{\lambda}$ the thermal conductivity, $\Delta \tilde{\theta}$ the reference temperature difference across the ice layer (defined here as $\Delta \tilde{\theta} = \tilde{\theta}_m - \tilde{\theta}_c$), \tilde{u}_{ref} the reference velocity and \tilde{h}_{ref} the reference length of the problem. In a real case scenario, heat diffusion is significantly faster than melting. This means that

the temperature distribution within the ice layer can quickly adapt to the motion of the interface and can always be considered in equilibrium state. It is therefore reasonable to assume that the time scale of heat diffusion, τ_D , is much smaller than the time scale of melting, τ_M . These two time scales can be defined as

$$\left\{ \begin{array}{l} \left| \frac{d\xi}{dt} \right| = \frac{\xi}{\tau_M}, \\ \left| \frac{\partial \theta}{\partial t} \right| = \frac{\Delta \theta}{\tau_D}, \end{array} \right. \quad (2.7)$$

where Δ is the characteristic temperature difference inside the ice layer (note that $\Delta \theta = 1$ by definition). The condition $\tau_M \gg \tau_D$, in combination with the system (2.1), yields

$$St \gg \frac{\Delta \theta \left| \frac{\partial \theta}{\partial z} + q_w \right|}{\xi \left| \frac{\partial^2 \theta}{\partial z^2} \right|} \approx \Delta \theta \frac{\Delta \theta / \xi + q_w}{\Delta \theta / \xi} \Rightarrow St \gg |1 + q_w \xi|. \quad (2.8)$$

When the condition (2.8) is satisfied, the following analytical solution for the problem (2.1) exists

$$\left\{ \begin{array}{l} \xi(t) = \frac{\theta_c}{q_w} \frac{S-1}{S} = \xi_{eq} \frac{S-1}{S}, \\ \frac{1}{S} + \ln |S| = \frac{1}{S_0} + \ln |S_0| - \frac{q_w^2}{\theta_c} \frac{t}{Pe St}, \\ S_0 = \frac{1}{1 - \xi_0 / \xi_{eq}}, \\ \theta(z, t) = \theta_c (1 - z / \xi(t)), \end{array} \right. \quad (2.9)$$

where $\xi_{eq} = \theta_c / q_w$ is the ice thickness at equilibrium. The reader is referred to [Appendix B](#) for a detailed derivation of this solution. The second equation in (2.9) can be used to obtain an estimate of the time required to reach the steady state, \mathcal{T}_{steady} . In principle, this equation predicts an infinite time since $S \rightarrow \infty$ (and $\ln |S| \rightarrow \infty$) for $\xi = \xi_{eq}$. Therefore, we define \mathcal{T}_{steady} as the time required to melt 99 % of all the ice that can melt once the equilibrium condition $\xi = \xi_{eq}$ is reached. When this condition is met, $\xi = \xi_0 - 0.99(\xi_0 - \xi_{eq})$, which yields $S^{-1} = 0.01(\xi_{eq} - \xi_0) / \xi_{eq}$ and, in turn,

$$\mathcal{T}_{steady} = \frac{\theta_c Pe St}{q_w^2} [0.99(1 - q_w \xi_0 / \theta_c) + \ln(0.01)]. \quad (2.10)$$

2.2. The two-phase Stefan problem

To complete the model and account for the heat transfer balance in the water layer, the heat flux $q_{S,w}$ that brings the meltwater to local thermal equilibrium with the bulk water must be included. This contribution is especially important at low St , when it is comparable to the latent heat q_L and cannot be neglected. In fact, if the assumption $q_{S,w} \approx 0$ is made (which is analogous to assuming a constant heat flux q_w applied directly to the interface, regardless of the velocity with which it evolves), the model predicts an instantaneous evolution of ξ to the equilibrium position in the limit $St \rightarrow 0$. In other words, the model predicts an infinite velocity of the ice–water interface at vanishing Stefan numbers. In reality, for small but finite values of St , the interface velocity is limited by thermal

diffusivity, which is responsible for the presence of $q_{S,w}$. In the case of ice melted by a turbulent flow of water, $q_{S,w}$ can be quantified as follows (in physical units)

$$\tilde{q}_{S,w} = \tilde{q}_b - \tilde{q}_w = (\tilde{\theta}_b - \tilde{\theta}_m) \tilde{\rho} \tilde{c}_p \frac{d\tilde{\xi}}{d\tilde{t}}, \quad (2.11)$$

with $\tilde{\theta}_b$ the bulk temperature of water. Equation (2.11) shows that $\tilde{q}_{S,w}$ can be interpreted as the heat flux required to bring the meltwater layer from the melting temperature $\tilde{\theta}_m$ to the bulk temperature $\tilde{\theta}_b$. In dimensionless form, (2.11) becomes

$$q_{S,w} = q_b - q_w = \underbrace{\left[\frac{(\tilde{\theta}_{bulk} - \tilde{\theta}_m) \tilde{\rho} \tilde{c}_p}{\tilde{\rho} \tilde{c}_p \Delta \tilde{\theta}} \right]}_{\mathcal{Q}} \underbrace{\left(\frac{\tilde{\rho} \tilde{c}_p \tilde{u}_\tau}{\tilde{\lambda}} \right)}_{Pe} \frac{d\xi}{dt} = \mathcal{Q} Pe \frac{d\xi}{dt}, \quad (2.12)$$

where $\tilde{\rho} \tilde{c}_p \Delta \tilde{\theta}$ is the reference sensible heat. Substituting (2.12) into (2.1) and assuming constant q_b yields a problem equal to that solved in the previous section, provided that St is now replaced by $\mathcal{Q} + St$ and q_w by q_b . Therefore, the analytical solution for the evolution of the ice layer thickness, ξ , is

$$\begin{cases} \xi(t) = \xi_{eq} \frac{S-1}{S}, \\ \frac{1}{S} + \ln |S| = 1 - \frac{\xi_0}{\xi_{eq}} - \ln \left| 1 - \frac{\xi_0}{\xi_{eq}} \right| - \frac{q_b^2}{\theta_c} t^*, \end{cases} \quad (2.13)$$

where $t^* = t/[Pe(St + \mathcal{Q})]$ is the rescaled time. The expression for the time required to reach the steady state, stemming from (2.10), becomes

$$\mathcal{T}_{steady} = \frac{\theta_c Pe (St + \mathcal{Q})}{q_b^2} [0.99(1 - q_b \xi_0 / \theta_c) + \ln 0.01]. \quad (2.14)$$

The accuracy of the model (2.13) has been verified by comparing its predictions with the numerical solution of the full set of (2.1). Details of the model assessment are provided in [Appendix B.1](#).

3. Simulation methodology

We consider a layer of ice capping a turbulent flow of warm water in a domain that, including the ice layer, has size $\tilde{L}_x \times \tilde{L}_y \times \tilde{L}_z = 2\pi \tilde{h} \times \pi \tilde{h} \times \tilde{h}$ along the streamwise (x), spanwise (y) and wall-normal (z) directions, respectively. During the simulations, the ice–water interface evolves dynamically as a result of ice melting and water freezing. To capture the dynamics of the system, we combine DNS of the Navier–Stokes and energy (EN) equations (Zonta, Sichani & Soldati 2022) with a phase-field method (Hester *et al.* 2020; Soligo, Roccon & Soldati 2021; Roccon, Zonta & Soldati 2023). The equations, and all the involved physical quantities, are made dimensionless using the height of the channel \tilde{h} , the temperature difference $\Delta \tilde{\theta}$ and the shear velocity $\tilde{u}_\tau = \sqrt{\tilde{\tau}_w / \tilde{\rho}}$, where $\tilde{\tau}_w$ is the average shear stress at the ice–water interface. The reader is referred to [Appendix A](#) for details on the non-dimensionalization of all flow variables.

3.1. Governing equations

The system of dimensionless governing equations reads as

$$\begin{cases} \frac{\partial \phi}{\partial t} = \frac{6}{5} \frac{1}{C Pe St} \left[\nabla^2 \phi - \frac{1-\phi}{\epsilon^2} \phi (1-2\phi + C\theta) \right], \\ \frac{\partial \theta}{\partial t} = \frac{1}{Pe} \nabla^2 \theta - \mathbf{u} \cdot \nabla \theta + St \frac{\partial \phi}{\partial t}, \\ \frac{\partial \mathbf{u}}{\partial t} = \frac{1}{Re_\tau} \nabla^2 \mathbf{u} - \mathbf{u} \cdot \nabla \mathbf{u} - \nabla p - \frac{\phi^2}{\eta_s} \mathbf{u}, \\ \nabla \cdot \mathbf{u} = 0. \end{cases} \quad (3.1)$$

The first equation in this system is the modified Allen–Cahn (AC) equation, used to track the evolution of the local ice volume fraction, ϕ . The second equation is the EN, used to track the evolution of the temperature field, θ . The last two equations are the Navier–Stokes and continuity equations, used to track the evolution of the velocity field, \mathbf{u} . The dimensionless groups that appear in (3.1) are the shear Reynolds number, the Péclet number and the Stefan number, defined as

$$Re_\tau = \frac{\tilde{u}_\tau \tilde{h}}{\tilde{\nu}}, \quad Pe = Re_\tau Pr = \frac{\tilde{\rho} \tilde{c}_p \tilde{u}_\tau \tilde{h}}{\tilde{\lambda}}, \quad St = \frac{\tilde{\mathcal{L}}}{\tilde{c}_p \Delta \tilde{\theta}}, \quad (3.2)$$

with $\tilde{\nu}$ the kinematic viscosity, $\tilde{\rho}$ the density, \tilde{c}_p the specific heat and $\tilde{\lambda}$ the thermal conductivity. For simplicity, we consider constant thermophysical properties across the two phases. The definitions of St and Pe given in (3.2) are analogous to those provided in § 2, with \tilde{u}_τ replacing \tilde{u}_{ref} and \tilde{h} replacing \tilde{h}_{ref} . This yields $Pe = Re_\tau Pr$ with $Pr = (\tilde{\rho} \tilde{c}_p \tilde{\nu})/\tilde{\lambda}$ the Prandtl number. The flow of water is driven by a mean pressure gradient imposed in the streamwise direction. Since the average height of the water layer, $\tilde{h}_w(t)$, increases over time due to melting, the effective Reynolds number of the flow, $Re_{eff} = \tilde{u}_\tau \tilde{h}_w / \tilde{\nu}$, changes accordingly and Re_τ corresponds to the maximum value that Re_{eff} can reach (when $\tilde{h}_w = \tilde{h}$). In the following, we indicate the initial value of the Reynolds number as $Re_{\tau,0}$ and its final value as $Re_{\tau,f}$, such that $Re_{\tau,0} \leq Re_{eff} \leq Re_{\tau,f}$. In the type of problem we decided to investigate, temperature is treated as a passive scalar and therefore buoyancy effects are negligible (Zonta & Soldati 2018).

The modified AC equation is used to implicitly describe the morphodynamic changes of the ice–water interface and is derived from a formulation of the phase-field method specifically designed for problems involving melting and solidification (Hester *et al.* 2020). The equation includes a source term on the right-hand side that depends on the local temperature θ , such that if the local temperature is below the freezing point, then ice is generated, while water is generated and the ice volume fraction is reduced if θ is above the melting point. The phase field method ensures a smooth transition between the ice phase (where $\phi = 1$) and the water phase (where $\phi = 0$) across a thin separation layer centred around the ice–water interface (where $\phi = 0.5$). The thickness of this layer is dictated by the phase field parameter, ϵ , which is imposed by computational requirements. In our simulations, $\epsilon = 0.005$, a value that corresponds to a layer approximately $0.04\tilde{h}$ thick. The parameter C appearing in the AC equation is the mobility coefficient of the phase-field method. From a physical point of view, this parameter is associated with the energy of the transition layer that separates the two phases. This energy (and, therefore, the value of C) affects the dependency of the temperature at the interface on the local curvature in conditions of thermodynamic

equilibrium (Gibbs–Thompson effect). Following Yang *et al.* (2023b) and Perissutti *et al.* (2024), we neglect the Gibbs–Thompson effect, since the curvatures of the ice–water interface are never large enough to make the interfacial temperature significantly different from the melting point. Numerically, this is achieved by setting $\mathcal{C} = 10$ (Perissutti *et al.* 2024). This value does not affect significantly the numerical stiffness of the problem, which increases with \mathcal{C} . In such conditions, the phase field formulation enforces the temperature to always be at the melting/freezing point ($\theta = 0$, as it follows from the definition of dimensionless temperature) at the ice–water interface. In the EN, a source term proportional to the time derivative of ϕ and to St is introduced to account for the contribution of the latent heat during melting and freezing. Following previous studies (Favier, Purseed & Duchemin 2019; Hester *et al.* 2020; Couston *et al.* 2021; Yang *et al.* 2022; Perissutti *et al.* 2024), a volume-penalization immersed boundary method (IBM) is used in combination with the Navier–Stokes equations. In this method, a source term is added in the momentum equations to force an exponential decay of the fluid velocity where the ice volume fraction is not zero. This decay is ruled by the time constant η_s , chosen as small as possible (7×10^{-4} in this study) to minimize the error between the exact solution of the Navier–Stokes equations and the IBM solution, which scales as $\sqrt{\eta_s}$ when compared with the sharp interface formulation (Favier *et al.* 2019), and prevent any velocity in the ice layer.

3.2. Numerical discretization and boundary conditions

The Navier–Stokes and continuity equations in the system (3.1) are rewritten in the wall-normal velocity–vorticity formulation (Canuto *et al.* 2007) and solved, together with the AC and EN equations, using a pseudospectral method that relies on discrete Fourier transforms along the homogeneous directions (x and y) and discrete Chebyshev transforms along the wall-normal direction (z). For this reason, the computational grid (consisting of $N_x \times N_y \times N_z$ points) is uniform in x and y , while Chebyshev–Gauss–Lobatto points are used in the z direction. The equations are advanced in time using an implicit–explicit scheme: the nonlinear terms are discretized using an Adams–Bashforth scheme, while for the linear terms, an implicit Euler scheme (for AC and EN) or a Crank–Nicolson scheme (for the wall-normal velocity–vorticity equations) is employed. More details about the numerical scheme can be found in Roccon (2024) and Roccon, Soligo & Soldati (2025). The solver is parallelized using a message passing interface (MPI) and leverages on a two-dimensional domain decomposition strategy. The code is also accelerated exploiting graphics processing units (GPUs) through OpenACC directives and CUDA Fortran instructions. The Nvidia cuFFT libraries are used to execute the Fourier/Chebyshev transforms.

As far as the boundary conditions are concerned, for the Navier–Stokes equation, a no-slip condition is enforced at the top boundary capping the ice layer, while a free shear condition is applied at the bottom boundary of the water layer,

$$\mathbf{i} \cdot \frac{\partial \mathbf{u}}{\partial z} \Big|_{z=0} = 0, \quad \mathbf{j} \cdot \frac{\partial \mathbf{u}}{\partial z} \Big|_{z=0} = 0, \quad \mathbf{k} \cdot \mathbf{u}(z=0) = 0, \quad \mathbf{u}(z=1) = \mathbf{0}. \quad (3.3)$$

Note that the velocity is zero throughout the ice layer since a no-slip condition is enforced at the ice–water interface by the IBM. In the EN, constant temperatures are imposed at both boundaries: above the melting point at the bottom boundary, $\theta(z=1) = 1$, and below the freezing point at the top one, $\theta(z=0) = -1$. The choice imposing a symmetric temperature difference between the top and bottom boundaries was made to be fully consistent with our previous work (Perissutti *et al.* 2024) and ensures that

Case	$Re_{\tau,0}$	$Re_{\tau,f}$	St	Pr	$N_x \times N_y \times N_z$	Regime	\mathcal{T}_{steady}	Relative computational cost
S1	170	189	0.1	1	$256 \times 256 \times 257$	Subcritical	18.19	1.00
S2	170	190	1.0	1	$256 \times 256 \times 257$	Subcritical	45.47	2.50
S3	170	190	10	1	$256 \times 256 \times 257$	Subcritical	318.29	17.50
S4	636	802	0.1	1	$512 \times 512 \times 513$	Supercritical	11.73	20.63
S5	636	803	1.0	1	$512 \times 512 \times 513$	Supercritical	29.33	51.60
S6	636	801	10	1	$512 \times 512 \times 513$	Supercritical	205.28	361.03

Table 1. Overview of the simulation parameters for each simulation (S1 to S6): Reynolds (initial and final), Stefan and Prandtl numbers, number of grid points (N_x , N_y , N_z), the ice morphology regime (subcritical or supercritical), the predicted time required for the average ice thickness to reach its steady-state value, \mathcal{T}_{steady} , and the estimated computational cost, normalized by the cost of the cheapest simulation, S1. One computational cost unit is roughly 50 GPU hours on a petascale Tier-0 supercomputer.

the ice–water interface remains inside the domain. We remark here that imposing an asymmetric temperature difference would only change the vertical equilibrium position of the ice interface inside the domain: no significant changes would be produced in the ice morphology. For the AC equation, no-flux conditions are applied at both boundaries,

$$\left. \frac{\partial \phi}{\partial z} \right|_{z=0} = 0, \quad \left. \frac{\partial \phi}{\partial z} \right|_{z=1} = 0. \quad (3.4)$$

These conditions prevent any unphysical flux of the ice phase through the domain boundaries and ensure that the changes in the volume fraction ϕ are only due to melting and freezing. Along the homogeneous directions (x and y), periodic boundary conditions are applied to all flow variables.

3.3. Simulation set-up

All simulations, summarized in [table 1](#), start from the same initial condition, which consists of an initially flat ice layer in the top part of the domain, from $z = 0.75$ to $z = 1$. The initial volume fraction is

$$\phi_0(x, y, z) = \frac{1}{2} \tanh \left(\frac{z - 0.75}{2\epsilon} \right) + \frac{1}{2}, \quad (3.5)$$

corresponding to the phase field equilibrium profile in the absence of melting and freezing. The interface position associated with (3.5) ensures that the interface is not too close to the channel centre (where the grid is coarser because of the Chebyshev nodes distribution), but the ice layer is still thick enough to properly catch the transient of the melting process. Below the flat ice layer, a fully developed turbulent flow is initialized by running a preliminary simulation in which ice melting is artificially suppressed, and the ice–water interface is kept flat and its thickness unchanged. This preliminary simulation is carried out until the statistically steady state is reached for the flow field. The steady-state flow is then used as the initial condition for the simulations with melting.

To conduct the study, two Reynolds numbers were simulated: one in the absence of the instability of the ice–water interface that leads to the formation of ice ripples (referred to as subcritical regime hereinafter, corresponding to a shear Reynolds number at the beginning of the simulation $Re_{\tau,0} = 170$) and one in which ice ripples form as a result of the interaction between ice streamwise advection and cross-stream diffusion of heat and momentum (referred to as supercritical regime hereinafter, corresponding to $Re_{\tau,0} = 636$). These values were chosen considering that the characteristic wavelength $\lambda_{x,cr}^+$ of the unstable disturbances in the flow should be larger than 2100 in wall units, with the fastest

growth rate being achieved at $\lambda_{x,cr}^+ \simeq 3500$ (Ashton & Kennedy 1972; Hsu *et al.* 1979). The corresponding (estimated) critical Reynolds numbers above which ice ripples are expected to form, are: $Re_{\tau}^{cr} = 251$ to have unstable modes, and $Re_{\tau}^{cr} = 418$ to have the fastest growing mode (Perissutti *et al.* 2024). It is worth mentioning that, at present, it is not possible to quantitatively predict a critical Reynolds number to discriminate between the two regimes based solely on the physical parameters of the system, primarily due to the difficulty of modelling with accuracy the phase shift between the heat flux and the ice–water interface (Perissutti *et al.* 2024). The phase shift is typically taken into account using empirical corrections (Thorsness, Morrisroe & Hanratty 1978), although recent studies have attempted to address this limitation (Chedevergne *et al.* 2023).

Table 1 shows $Re_{\tau,0}$ together with the effective Reynolds number at the end of the simulation ($Re_{\tau,f}$). For each value of the Reynolds number, we simulated three different Stefan numbers to evaluate the effect of the latent heat contribution. We already anticipated in § 2 that the main effect of St is to change the time required to reach the steady state, \mathcal{T}_{steady} and that, at large St , \mathcal{T}_{steady} (and therefore the computational cost) becomes significantly higher. For this reason, table 1 also shows the value of \mathcal{T}_{steady} for each simulation as obtained from (2.14). Note that \mathcal{T}_{steady} is calculated assuming a constant heat flux q_b through the bottom of the domain: $q_b = -6.2$ at $Re_{\tau,0} = 170$ and $q_b = -19$ at $Re_{\tau,0} = 636$, in dimensionless units. These values were obtained directly from the DNS data. The tabulated values of \mathcal{T}_{steady} allow to estimate the computational cost needed to reach the equilibrium ice thickness. For this estimation, we took as reference a petascale Tier-0 supercomputer equipped with four GPUs per node and assumed perfect weak scalability (which is indeed what we observed within the range of MPI tasks employed for each simulation). Note that the computational cost is relative to the cheapest simulation (S1) and one computational cost unit is roughly equivalent to 50 GPU hours. We remark here that reaching the equilibrium ice thickness does not necessarily imply reaching a statistically steady state for the ice morphology, which is what we want to examine. For this reason, simulation runs were conducted beyond the equilibrium condition, implying that their effective cost is larger than that presented in table 1.

4. Morphodynamics of ice melting

Figure 2 shows the physical domain considered to perform the simulations in the subcritical regime (figure 2a, $Re_{\tau,0} = 170$) and in the supercritical regime (figure 2b, $Re_{\tau,0} = 636$) at $St = 1$. The imposed boundary conditions and the domain size in wall units (w.u.) are also reported. Note that the size of the computational domain scales with $Re_{\tau,0}$. Therefore, the domain in the supercritical regime is roughly 50 times larger than in the subcritical regimes, volumewise. Water, shown in blue, flows underneath the ice (shown in white) from left to right. The ice–water interface is given by the $\phi = 0.5$ isosurface and is kept at melting temperature θ_m . Water is warmer (light blue regions) near the bottom of the domain, where a constant dimensionless temperature $\theta = 1$ is imposed. Warm water is brought by turbulent convection to the bulk region of the domain, where it mixes with the cold water (dark blue regions) coming from the near-interface region. Mixing results in a bulk water temperature of $\theta_b \simeq 0.5$ (and, hence, $\mathcal{Q} = 0.5$) and provides a heat flux input, represented by q_b , to the ice–water interface. When q_b is larger than the heat flux q_t through the ice layer, melting takes place and the average thickness of the ice layer, $\langle \xi \rangle$, decreases over time. Angular brackets indicate an average in space, along both x and y . As already mentioned in § 2, the excess of heat contributes not only to ice melting (latent heat) but also warms up the ice that is about to melt as well as the meltwater (sensible heat). When $q_b = q_t$, the system is at steady state and the average thickness remains

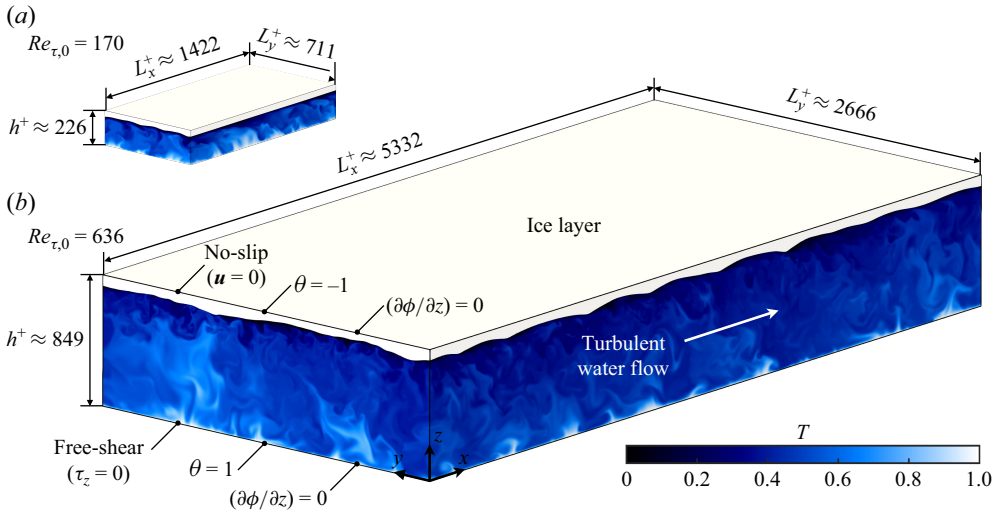


Figure 2. Rendering of the physical domain considered for the simulations at $Re_{\tau,0} = 170$ (a) and $Re_{\tau,0} = 636$ (b). The domain is open at the bottom (where a free-shear condition is applied), while an ice layer (in white) caps a water layer (in blue) that flows from left to right beneath the ice. The colourmap shows the regions of lower temperature, in dark blue, and those of higher temperature, in light blue, at $St = 1$.

constant over time. Locally, however, the interface is always characterized by a complex morphology that dynamically changes over time: this happens because the heat exchange between ice and water is modulated by turbulence. To highlight the phenomenology of the interface morphodynamics and better understand the role of turbulence, we discuss first the results in the subcritical regime ($Re_{\tau,0} = 170$), focusing on the effect of St . In particular, we compare the overall melting dynamics with the 1-D model presented in § 2 and quantify the space- and time-dependent features of the ice–water interface, $\xi(x, y, t)$. The same analysis is then carried out for the supercritical regime ($Re_{\tau,0} = 636$), with particular attention to the formation and dynamics of the ice ripples.

4.1. Morphodynamics in the subcritical regime

Figure 3 shows the ice layer for $Re_{\tau,0} = 170$ and $St = 1$ at statistically steady state. The layer is flipped upside down to better visualize the ice–water interface. In this case, the ice morphology is characterized by crests and valleys oriented in the streamwise direction (referred to hereinafter as turbulence-driven ice streaks) and separated by a characteristic wavelength λ_y . Figure 4 shows the effect of the Stefan number on the ice morphology, more specifically on the fluctuating component of the ice thickness, $\xi'(x, y, t) = \xi(x, y, t) - \langle \xi \rangle$, is plotted for $St = 0.1$ (figure 4a), $St = 1$ (figure 4b) and $St = 10$ (figure 4c) at steady state. All the panels refer to the same rescaled time t^* , defined in § 2. As it will be clarified later, the main features of the melting dynamics scale consistently with t^* . The turbulence-driven ice streaks are clearly visible over the range of St we considered and their topological features do not change much with St . As reported by Perissutti *et al.* (2024), these structures are directly generated by turbulence and should not in principle be affected by a change in the latent heat flux. The non-uniform heat flux provided by the near-wall fluid velocity streaks allows the ice crests and valleys to mark their footprint on the ice–water interface. However, some quantitative differences among the three cases can be observed. First, the maximum amplitude of the ice thickness fluctuations, ξ' , decreases as St increases and the interface appears to be

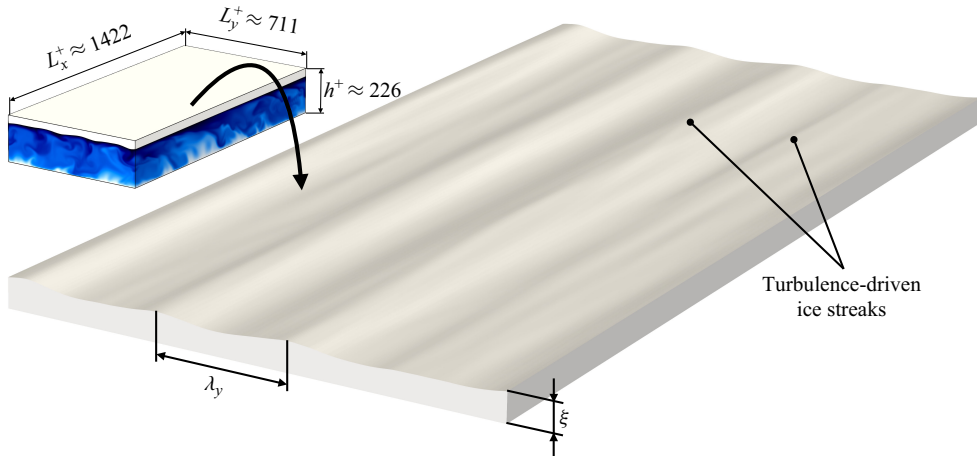


Figure 3. Visualization of the ice layer, flipped upside down to highlight the interface morphology, in the subcritical regime ($Re_{\tau,0} = 170$) and $St = 1$. In this regime, the ice morphology is characterized by turbulence-driven ice streaks that are aligned along the streamwise direction and separated by a characteristic wavelength λ_y .

somewhat smoother in the streamwise direction, with ξ' that remains almost unchanged along the x direction. Conversely, at low St , the irregularity of the interface becomes stronger and changes in ξ' become noticeable also along the streamwise direction. This behaviour is due to the fact that a larger latent heat contribution (i.e. larger St) reduces the volume of ice that is melted (or frozen) locally by the heat flux fluctuations induced by turbulence, reducing in turn the amplitude of ξ' . This also has a time-filtering effect on the modifications of the ice thickness: a short pulse of high heat flux is less impactful on the final ice morphology and allows the latter to become more regular. The crest-to-trough height of the ice streaks ranges between roughly 5 and 15 w.u., a value large enough to allow dynamic interactions with the turbulent structures of the flow. These interactions cause the streamwise-oriented ice streaks to meander sideways, in a way that is similar to what the near-wall fluid velocity streaks do (Marchioli & Soldati 2002), albeit to a lesser extent. This can be explained considering that turbulent streaks are free to move sideways near a non-evolving flat wall, not equally so in the presence of ice streaks. Low-speed streaks of fluid tend to remain linked to the ice crests, while high-speed streaks tend to form more often in the troughs. This creates a self-reinforcing mechanism that pins the turbulent streaks by hindering their meandering and sustains the ice morphodynamics by increasing the clearance between crests and troughs. The correlation between ice crests and low-speed streaks (or equivalently, valleys and high-speed streaks) becomes stronger at lower St , because the typical time scales with which the interface evolves become shorter and hence closer to those of the fluid velocity streaks. The stronger the correlation, the larger the height difference between crests and troughs, explaining why they become more prominent at low St .

Figure 5 shows the evolution of the average ice thickness, $\langle \xi \rangle$, as a function of the rescaled time, t^* . The model discussed in § 2 predicts that, with such rescaling, the melting process should evolve independently of St and should follow the behaviour indicated by the black dashed line, which corresponds to the analytical solution of (2.13) that can be obtained when q_b is provided. Here, we used $q_b = -6.2$, a value obtained directly from the simulations. For $St = 1$ and $St = 10$, the model captures well the evolution of the average ice thickness, while the prediction is just slightly worse for $St = 0.1$. Note that

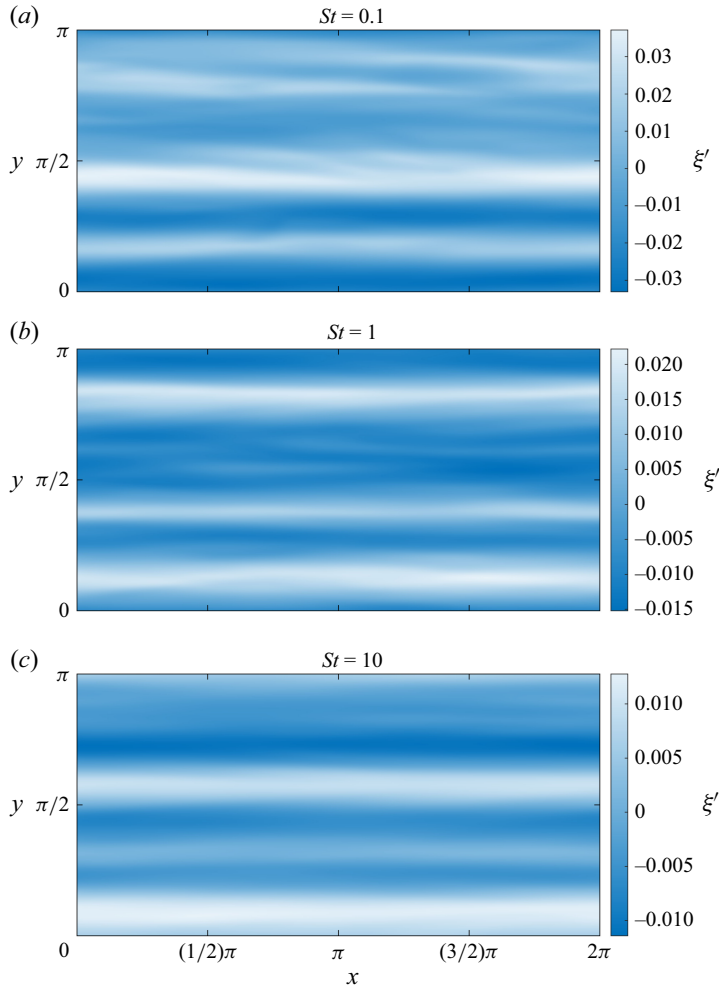


Figure 4. Influence of St on ice morphology in the subcritical regime ($Re_{\tau,0} = 170$). The spatial distribution of the ice thickness fluctuation, $\xi' = \xi - \langle \xi \rangle$, at steady state is shown for $St = 0.1$ (a), $St = 1$ (b) and $St = 10$ (c). The snapshots refer to the same rescaled time ($t^* = 0.17$). Thicker ice regions are shown in white, thinner ice regions in blue. The ice morphology is not dramatically affected by St , yet some differences among the three cases can be noticed. At low St , the ice morphology is characterized by slight variations of ξ' along the streamwise direction, these variations being damped at high St .

this value is rather close to the lower bound for the range of Stefan numbers within which the model is expected to perform reliably. The lower bound can be estimated using the condition (2.8), which yields $St \gg 0.05$ for the subcritical case, based on the initial value of the ice thickness. In spite of this, the model prediction is still fairly accurate, as also discussed in Appendix B. At the lower Stefan number, melting takes place very quickly in the early stages, while progressively slowing as the equilibrium condition, $\langle \xi \rangle = \langle \xi_{eq} \rangle$, is approached (at time $\mathcal{T}_{steady}^* \approx 0.134$). This behaviour can be understood considering that the effects of heat diffusivity are more important at low St , and melting is mainly counteracted by the conductive heat flux through the ice layer. This heat flux is weak at the beginning of the simulation, when the ice layer is thick, but becomes stronger as ice gets thinner on a time scale that is dictated by the thermal diffusivity. At larger Stefan numbers ($St = 1$ and $St = 10$), the latent heat flux is strong enough to overcome the effect

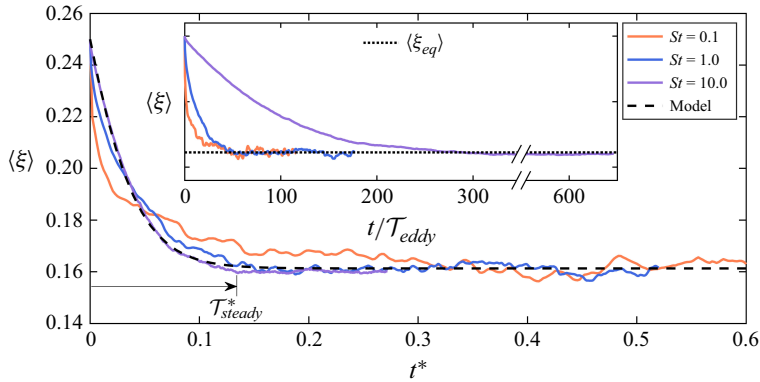


Figure 5. Time evolution of the average ice thickness, $\langle \xi \rangle$, at $Re_{\tau,0} = 170$ for $St = 0.1$ (orange line), $St = 1$ (blue line) and $St = 10$ (purple line) as a function of the rescaled time t^* . The prediction from the analytical model is also shown (black dashed line). The model predicts a rescaled steady-state time equal to $\mathcal{T}_{steady}^* \approx 0.134$, also shown in the figure. The inset shows the evolution of the ice thickness when time is normalized by the eddy turnover time of the flow, \mathcal{T}_{eddy} , rather than rescaled using Pe and St .

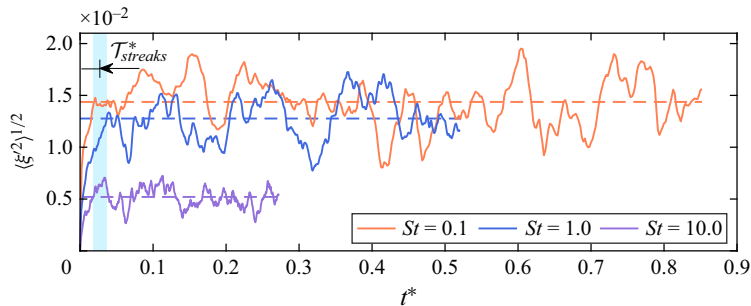


Figure 6. Time evolution of the ice fluctuation amplitude (i.e. the standard deviation of the ice thickness) $\langle \xi'^2 \rangle^{1/2}$ at $Re_{\tau,0} = 170$ for $St = 0.1$ (orange line), $St = 1$ (blue line) and $St = 10$ (purple line). In all cases, a statistically steady state is reached eventually, albeit at different times, ranging from 0.018 to 0.036 depending on St (as indicated by the light blue vertical band in the figure). This range defines the characteristic time scale of the turbulence-driven ice streaks formation, $\mathcal{T}_{streaks}^*$, in the subcritical regime. To allow a more direct comparison between the different time scales at play, in the following we take $\mathcal{T}_{streaks}^* \approx 0.027$, which is the average value among the different cases. Note that, even at steady state, $\langle \xi'^2 \rangle^{1/2}$ oscillates significantly around the averages steady-state value (marked for each case with a dashed line of the corresponding colour). For $St = 10$, the standard deviation is significantly lower ($\langle \xi'^2 \rangle^{1/2} \approx 0.0052$) compared with the other two cases ($\langle \xi'^2 \rangle^{1/2} \approx 0.0128$ for $St = 1$ and $\langle \xi'^2 \rangle^{1/2} \approx 0.0143$ for $St = 0.1$).

of thermal diffusivity (which is neglected in the model) and produce a slower and more gradual melting, in better agreement with the theoretical prediction. The inset of figure 5 shows the evolution of $\langle \xi \rangle$ without rescaling: time is normalized by the eddy turnover time $\mathcal{T}_{eddy} = h/u_\tau$ to highlight the dependence of the melting time scale on St . The simulation at $St = 10$ is the one that takes longer to reach the steady state for $\langle \xi \rangle$ (roughly 300 eddy turnover times) and, hence, is the one that is computationally more expensive: the simulated time span covers over 600 eddy turnover times, almost three times that of the $St = 1$ simulation and almost 10 times that of the $St = 0.1$ simulation.

Although the average ice thickness reaches an equilibrium condition, the local ice thickness continues to change over time while remaining in a statistically steady state. This is shown in figure 6, where the instantaneous standard deviation of the ice thickness,

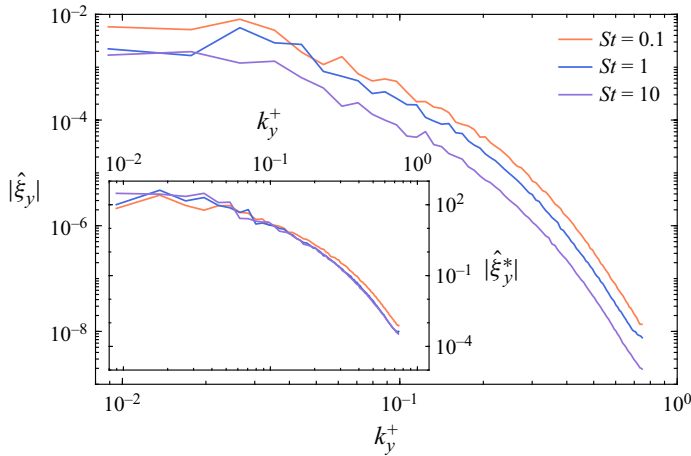


Figure 7. Spanwise spectra of the ice layer thickness, $|\hat{\xi}_y|$, in the subcritical regime ($Re_{\tau,0} = 170$) for $St = 0.1$ (orange), $St = 1$ (blue) and $St = 10$ (purple). All the spectra are averaged along the streamwise direction and in time, over a short time interval $\Delta t^* = 0.034$ centred at time $t^* = 0.17$, taken at steady state. As shown in the inset, the spectra overlap almost perfectly when rescaled as $|\hat{\xi}_y^*| = Pe\sqrt{St + Q}|\hat{\xi}_y|$.

$\langle \xi'^2 \rangle^{1/2}$, is plotted over the rescaled time t^* . After a short initial transient, the standard deviation oscillates around a value that remains roughly constant over time. Because the turbulence-driven ice streaks are the only structures observed at low $Re_{\tau,0}$, the extent of the transient may be interpreted as the characteristic time required to form the streaks, $\mathcal{T}_{streaks}^*$. Here, we assume that the transient ends as soon as the standard deviation first crosses its mean value at steady state. The crossover occurs at slightly different times, depending on St , within a range 0.018–0.036 (with average value equal to 0.027) that is highlighted by the light blue vertical band in figure 6. This range defines the characteristic time scale of the turbulence-driven ice streaks formation, $\mathcal{T}_{streaks}^*$, in the subcritical regime, which is roughly five times shorter than the steady-state time \mathcal{T}_{steady}^* shown in figure 5. This indicates that the mechanism by which the ice streaks are generated, acts on time scales that are significantly shorter than those needed to reach the equilibrium condition. Figure 6 also confirms that the ice interface is less deformed at higher St , as observed qualitatively in figure 4. The average value of the standard deviation at $St = 10$ is $\langle \xi'^2 \rangle^{1/2} \approx 0.0052$, significantly lower than in the other two cases, which are fairly similar: $\langle \xi'^2 \rangle^{1/2} \approx 0.0128$ at $St = 1$ and $\langle \xi'^2 \rangle^{1/2} \approx 0.0143$ at $St = 0.1$, respectively. This observation suggests that morphological changes of the interface are dominated by the latent heat effect at higher St , whereas the heat diffusivity is predominant at lower St . To further analyse the interface morphology, in figure 7 we show the spanwise spectra of the ice thickness, $|\hat{\xi}_y|$. These spectra are obtained by averaging along the streamwise direction and over a short time interval $\Delta t^* = 0.034$ centred at time $t^* = 0.17$. They are plotted as a function of the spanwise wavenumber in w.u., $k_y^+ = k_y/Re_\tau$, with $k_y = 2\pi/\lambda_y$. All spectra exhibit roughly the same decaying trend, with differences in amplitude that become smaller as St increases. This behaviour is consistent with previous observations and is confirmed by the inset of figure 7, which clearly shows that the spectra nicely overlap when rescaled by the Péclet and Stefan numbers as $|\hat{\xi}_y^*| = Pe\sqrt{St + Q}|\hat{\xi}_y|$. This scaling relation was obtained empirically from the collapse of the rescaled spectra. Further investigation, for instance focused on the dynamical nature of the turbulence-driven ice streaks, is needed to provide a theoretical background for the $Pe\sqrt{St + Q}$ scaling.

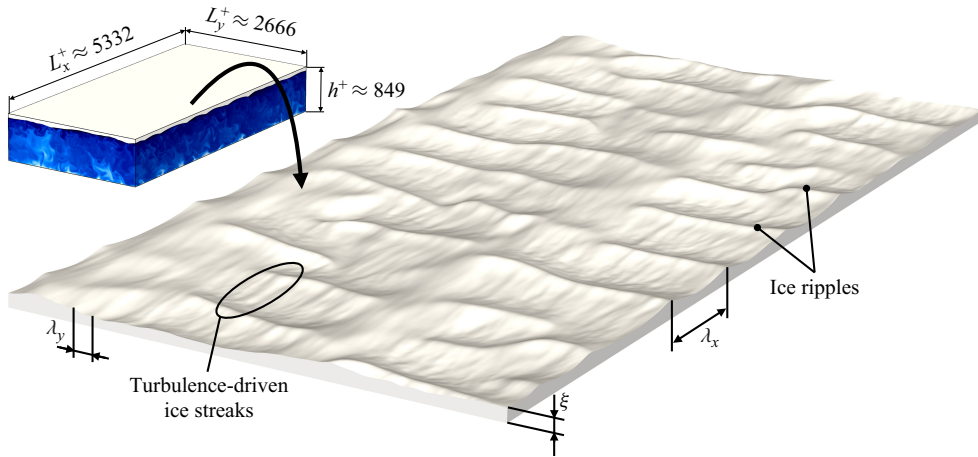


Figure 8. Visualization of the ice layer (flipped upside down to highlight the interface morphology) in the supercritical regime ($Re_{\tau,0} = 636$) at $St = 1$. This regime is characterized by the presence of turbulence-driven ice streaks, having a characteristic wavelength λ_y , and observed also in the subcritical regime, superposed to wavy ice ripples aligned with the spanwise flow direction, having a characteristic wavelength λ_x .

4.2. Morphodynamics in the supercritical regime

The analysis carried out for the subcritical regime is applied here to the supercritical regime. In figure 8, we show an instantaneous visualization of the ice–water interface (flipped upside down to highlight its main morphological features) in the supercritical regime ($Re_{\tau,0} = 636$) at $St = 1$. First, it can be observed that the ice layer is thinner than in the subcritical regime, due to the highest heat flux resulting from the stronger turbulence of the water flow. In addition, the ice morphology appears more complex than in the subcritical regime due to the superposition of the turbulence-driven ice streaks with wave-like ripples of greater length scale that develop orthogonally to the flow direction. These structures are characterized by sharp crests separated by a wavelength, λ_x , and exhibit a quasiperiodic behaviour along the streamwise direction. Ice ripples typically form as a result of a morphodynamic instability that emerges only at high Reynolds numbers. The sharpness of the crest, separated by concave depressions, is in line with what is observed in dissolution patterns and can be explained solely by geometric arguments stemming from the surface evolution (Chaigne *et al.* 2023).

Similar to the subcritical regime, the interface morphology is mildly affected by St , as shown in figure 9, where the fluctuating component of the ice thickness, ξ' , is reported for $St = 0.1$ (figure 9a), $St = 1$ (figure 9b) and $St = 10$ (figure 9c). All plots refer to the same time instant, equal to the time at which the ice ripples are observed to reach their maximum height, $t^* \approx 0.0156$. By visual inspection of figure 9, it is possible to appreciate that the main morphological features of the ice–water interface do not change dramatically with St : in all three cases, the ice–water interface is mainly characterized by the presence of ice ripples that have fairly similar wavelength and amplitude. The latter, in particular, can reach values of the order of 70–80 w.u., while the typical wavelength ranges between ≈ 530 and ≈ 670 w.u. These values are significantly lower than the minimum wavelength required for the onset of instability. This wavelength can be estimated using the models proposed in the literature, e.g. the model developed by Hanratty (1981), which predicts a minimum wavelength of approximately 1500 w.u., or the more recent model by Chedeveigne *et al.* (2023), which predicts a minimum wavelength of approximately 1000 w.u. This discrepancy might be due to the finiteness of the computational domain in

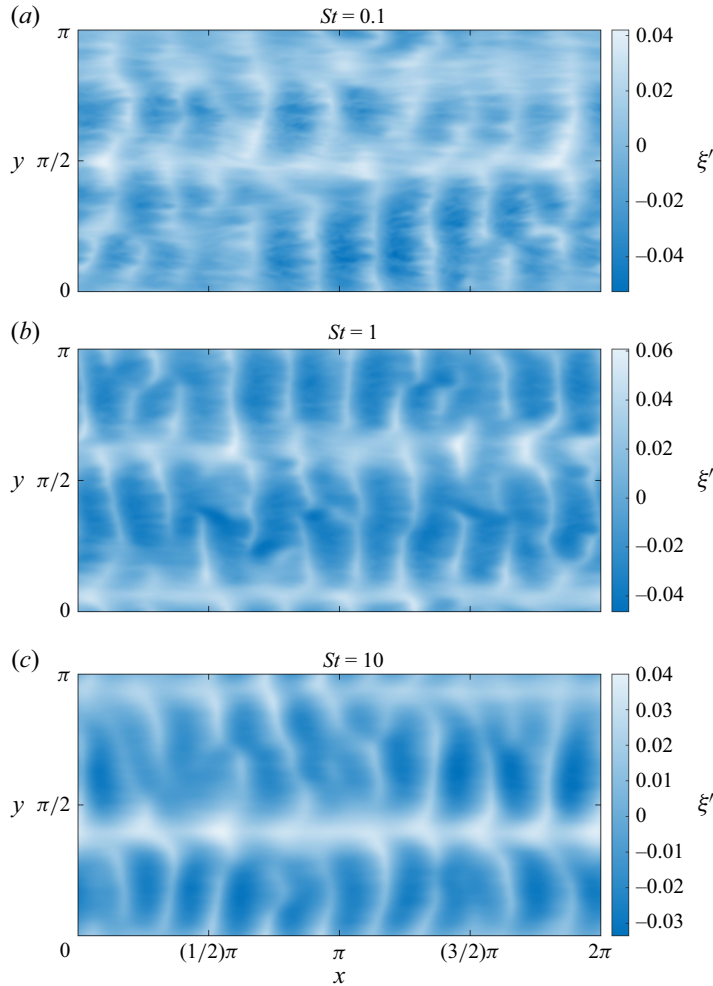


Figure 9. Influence of St on ice morphology in the supercritical regime ($Re_{\tau,0} = 636$). The fluctuating component of the ice thickness map, $\xi' = \xi - \langle \xi \rangle$, is shown for $St = 0.1$ (a), $St = 1$ (b) and $St = 10$ (c). All plots are taken at the rescaled time $t^* \approx 0.0156$, which is when the amplitude of the ice ripples is observed to become the highest. Thicker ice regions are shown in white, thinner ice regions in blue. For all St , the supercritical morphology is characterized by the presence of ice ripples, which are fairly similar in shape. The main effect of St is to reduce the size of the superposed turbulence-driven ice streaks, which are less visible at high St .

the wall-normal direction: the maximum size of the vortical structures is constrained by the channel height, h , favouring the development of lower wavelengths. Nonlinear effects that the models are unable to capture may also explain the different values. Note that the streamwise length of the computational domain in the subcritical regime is equal to 1420 w.u. and is sufficient to accommodate at least two ripple wavelengths as measured in the supercritical regime. Considering that such wavelengths were found to be independent of the flow Reynolds number when expressed in wall units (Hsu *et al.* 1979; Thomas 1979), it seems reasonable to conclude that the lack of ice ripples in the subcritical regime is not related to the computational domain size.

Despite the limited St effects, figure 9 shows some interesting modifications: at high St , the ice ripples seem less blurred, most likely because the latent heat flux acts as a temporal filter and mitigates the effect of the heat fluctuations on the interface. Another reason

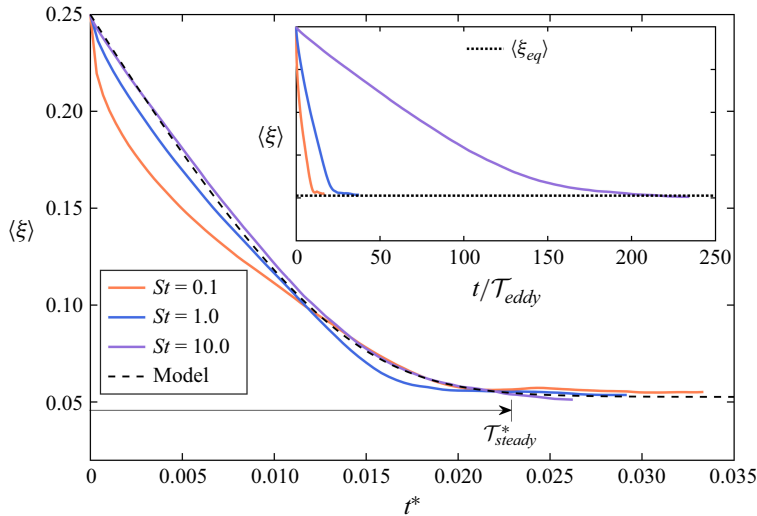


Figure 10. Time evolution of the average ice thickness, $\langle \xi \rangle$, at $Re_{\tau,0} = 636$ for $St = 0.1$ (orange), $St = 1$ (blue) and $St = 10$ (purple). The prediction of the analytical model is represented by the black dashed line. The steady-state time predicted by the model is also shown: $\mathcal{T}_{steady}^* \approx 0.023$. Similarly to the subcritical case, the prediction is fairly accurate for large St , while becoming less precise for low St . The inset shows the evolution of the ice thickness when time is normalized by the eddy turnover time, \mathcal{T}_{eddy} , rather than rescaled using Pe and St .

may be that, while the amplitude of ice ripples seems unaffected by St , the depth of the overlapping turbulence-driven ice streaks does depend on St , as discussed in the previous section. This results in a smaller height of the turbulence-driven ice streaks relative to the size of the ice ripples, which appear more defined.

Figure 10 shows the evolution of the average ice layer thickness, $\langle \xi \rangle$, as a function of the rescaled time, t^* . The model prediction, obtained solving (2.13) with $q_b = -19$ as provided by the numerical simulation, is again indicated by the black dashed line. Similarly to the subcritical case, the accuracy of the model improves with increasing St : indeed, the simulation at $St = 10$ (purple line) matches very well with the model prediction. The prediction for $St = 1$ (blue line) is still fairly accurate, indicating that the effect of the latent heat becomes predominant: melting slows down and the evolution of $\langle \xi \rangle$ becomes linear in time. Differences become more significant at $St = 0.1$ since, in this case, the condition (2.8) predicts that the model is accurate if $St \gg 1.35$. This is evident especially during the early stages of the interface evolution, when fast melting occurs due to heat diffusivity effects and the error of the model is large because the interface is still far from equilibrium (see Appendix B). Similarly to the subcritical case, as the interface approaches equilibrium, the error decreases, allowing the model to provide reasonably accurate predictions even for $St = 0.1$ and $St = 1$. Note that, for the case $St = 1$, the melting rate (given by the slope of the curves in figure 10) is larger than the value predicted by the model within the time interval from $t^* \approx 0.01$ and $t^* \approx 0.015$. As it will be shown later, this is the time window within which the ice ripples reach their maximum amplitude. Interestingly, the model is always able to capture correctly the equilibrium ice thickness, $\langle \xi_{eq} \rangle$, which is independent of St and has the same value in all the simulations.

The rescaled steady-state time required to reach the equilibrium is also similar in all the three cases: $\mathcal{T}_{steady}^* \approx 0.023$, computed from (2.14). This implies that the model can capture with acceptable accuracy the relevant time scales of the melting process even in the supercritical regime. Note that, if no time rescaling is considered, then these time scales

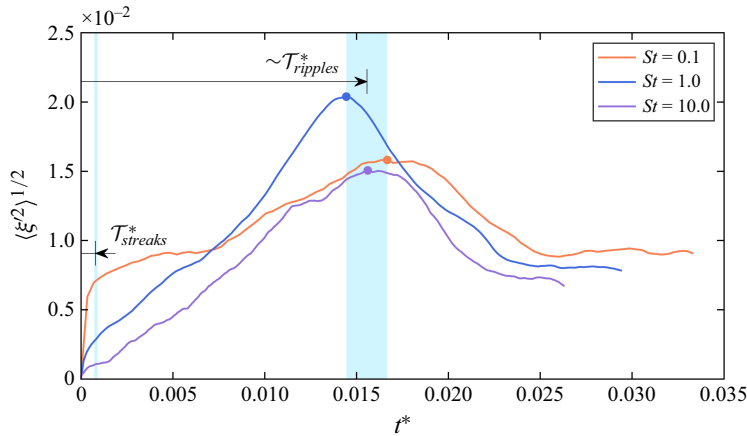


Figure 11. Time evolution of the ice fluctuation amplitude (equal to the standard deviation of the ice thickness), $\langle \xi^2 \rangle^{1/2}$, in the supercritical regime ($Re_{\tau,0} = 636$) for $St = 0.1$ (orange), $St = 1$ (blue) and $St = 10$ (purple). Due to the presence of the ice ripples, $\langle \xi^2 \rangle^{1/2}$ grows until reaching a maximum value (marked by a dot for each case). The maximum value of $\langle \xi^2 \rangle^{1/2}$ is attained within a time window (highlighted by the light blue vertical band) centred at $t^* \approx 0.0156$. This value represents the characteristic time scale required to fully form the ripples and is indicated as $\mathcal{T}_{ripples}^*$ in the figure. Once the maximum amplitude is attained, $\langle \xi^2 \rangle^{1/2}$ decreases until the steady state is reached (at different times depending on St). The time required to form the turbulence-driven ice streaks (also shown) is much shorter than the ice ripples time scale: $\mathcal{T}_{streaks}^* \approx 8.14 \cdot 10^{-4}$.

are much bigger for larger St , as shown in the inset of figure 10, where $\langle \xi \rangle$ is plotted as a function of the non-rescaled time t normalized by the eddy turnover time, \mathcal{T}_{eddy} . The inset shows that, as in the subcritical regime (see discussion of figure 5), the most expensive simulation from a computational point of view is the one at $St = 10$, which covers almost 250 eddy turnover times.

A notable difference between the subcritical and supercritical regimes is that, in the latter regime, the standard deviation, $\langle \xi^2 \rangle^{1/2}$, does not simply oscillate around a constant, steady-state value but rather exhibits an initial growth followed by a decrease before reaching the steady state, as shown in figure 11. The fluctuation amplitude grows until a maximum value (highlighted by the dot in each curves) is reached. The maximum is reached at different times depending on St , but within a relatively narrow time range (marked with the light blue region in the figure), centred at $t^* \approx 0.0156$. This value represents the characteristic time scale required to fully form the ripples (see also discussion of figure 9). Once the maximum amplitude is attained, $\langle \xi^2 \rangle^{1/2}$ decreases until the steady state is reached (again, at different times depending on St). This behaviour can be understood considering that the fluctuation amplitude is influenced not only by the presence of the turbulence-driven ice streaks, as is the case in the subcritical regime, but also (mostly, in fact) by the ice ripples, which are much larger in size and hence more impactful on the behaviour of $\langle \xi^2 \rangle^{1/2}$. As will be detailed in § 4.3, we can anticipate that ice ripples undergo the same dynamics (initial growth, maximum amplitude, subsequent decay), suggesting that the peak of $\langle \xi^2 \rangle^{1/2}$ and the maximum amplitude of the ice ripples occur approximately at the same time, namely $\mathcal{T}_{ripples}^*$.

The trends shown in figure 11 do not allow a straightforward quantification of the time scale required to form the turbulence-driven ice streaks, $\mathcal{T}_{streaks}^*$, in the supercritical regime. Due to the presence of the ripples, $\mathcal{T}_{streaks}^*$ cannot be simply set equal to the steady-state time for $\langle \xi^2 \rangle^{1/2}$, as done for the subcritical regime, see figure 6. The reason is that the steady state is reached only when the ice ripples stabilize. The alternative

definition we adopted in this case is to set $\mathcal{T}_{streaks}^*$ equal to the steady-state time for the spanwise-spectrum amplitude of the ice interface, $|\hat{\xi}_y|$. This spectrum is evaluated at the wavenumber that corresponds to the typical wavelength of the turbulence-driven ice streaks ($\lambda_y^+ \approx 100$), not shown here for brevity. More specifically, for each case, $\mathcal{T}_{streaks}^*$ is set equal to the rescaled time at which $|\hat{\xi}_y|_{\lambda^+=100}$ first falls within 5 % of its time-averaged value (computed from $\mathcal{T}_{streaks}^*$ onward). This results in a narrow range of values of $\mathcal{T}_{streaks}^*$, centred around 8.14×10^{-4} , between the different simulations, highlighted by the light blue vertical band in figure 11. In the supercritical case, the difference between \mathcal{T}_{steady}^* and $\mathcal{T}_{streaks}^*$, corresponding to a ratio $\mathcal{T}_{steady}^*/\mathcal{T}_{streaks}^* \approx 30$, is larger than in the subcritical case, where corresponding to a ratio $\mathcal{T}_{steady}^*/\mathcal{T}_{streaks}^* \approx 5$. This is likely due to the size of the turbulence-driven ice streaks, which is significantly smaller than the domain size (which increases linearly with $Re_{\tau,0}$ in each flow direction) in the supercritical case. The time scale of the turbulence-driven ice streaks is also much smaller than that of the ice ripples, $\mathcal{T}_{ripples}^*$, their ratio being $\mathcal{T}_{ripples}^*/\mathcal{T}_{streaks}^* \approx 20$. This indicates that the two phenomena are well separated in time and are governed by independent physical mechanisms. We also notice that the steady-state value of $\langle \xi'^2 \rangle^{1/2}$ is attained between $t^* \approx 0.023$ and $t^* \approx 0.025$, which is approximately the same time at which the steady state for $\langle \xi \rangle$ is reached (see value of \mathcal{T}_{steady}^* in figure 10).

As mentioned, it is not possible to filter out the effect of the ice ripples on the ice thickness fluctuations from figure 11. To isolate and characterize the effect of the turbulence-driven ice streaks, we thus examine the spanwise spectra shown in figure 13. These spectra are unaffected by the presence of the ripples, which induce significant interface deformations along the streamwise direction only. As done in figure 7, spectra are averaged in space (along x) and time, over a time interval $\Delta t^* = 0.003$ centred at $t^* = 0.0156 \equiv \mathcal{T}_{ripples}^*$: within this interval, the ice ripples reach their maximum amplitude regardless of St . Figure 13 shows clearly that, also in the supercritical regime, spanwise spectra share the same decaying trend and overlap nicely when rescaled as $|\hat{\xi}_y^*| = |\hat{\xi}_y|Pe\sqrt{St + Q}$ (see figure inset). Additionally, the inset shows the rescaled spectra for the subcritical cases (dashed lines), which collapse on top of the simulations at $Re_{\tau,0} = 636$. This indicates that the morphology of the turbulence-driven ice streaks is similar over the range of St investigated in our study, but also over the range of $Re_{\tau,0}$ (namely Pe) characterizing the different regimes. The emergence of ripples does not affect the spanwise features of the ice–water interface, but increases the variability of the interface morphology along the streamwise direction, as confirmed by the streamwise spectra, $|\hat{\xi}_x|$, shown in figure 12. These spectra are averaged in space, along the spanwise direction, and in time, over the same interval of figure 13. Three peaks, indicating the presence of the ice ripples, are clearly visible at slightly different values of the dimensionless streamwise wavenumber, k_x : more precisely, $k_{x,max} = 8$, $k_{x,max} = 10$ and $k_{x,max} = 9$ for $St = 0.1$, $St = 1$ and $St = 10$, respectively. Note that no peak is observed in the subcritical spectra ($Re_{\tau,0} = 170$), shown with dashed lines in the inset of figure 12. Recalling that $k_x^+ = k_x/Re_\tau = 2\pi/\lambda_x^+$ and $L_x^+ = 2\pi Re_\tau$, it follows that the supercritical peak values of $|\hat{\xi}_x|$ correspond to characteristic wavelengths of the ripples $\lambda_x^+ = L_x^+/8$, $L_x^+/10$ and $L_x^+/9$. Once rescaled, these wavenumbers cover a narrow range of values centred at $k_x^+ = k_x/Re_\tau \approx 10^{-2}$: this implies that λ_x is weakly affected by St , confirming the qualitative observations drawn from figure 9. Also poorly affected by the Stefan number is the amplitude of the ice ripples, given that the peak values of $|\hat{\xi}_y|$ are almost identical in the three simulations: $|\hat{\xi}_x|_{max} \approx 3 \times 10^{-3}$.

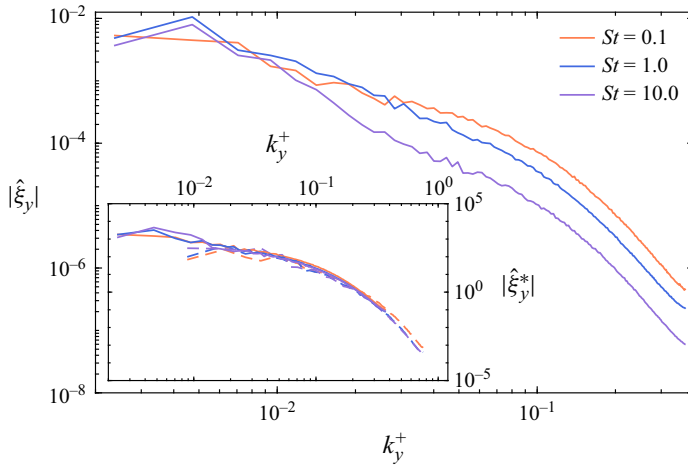


Figure 12. Streamwise spectra of the ice thickness, $|\hat{\xi}_y|$, in the supercritical regime ($Re_{\tau,0} = 636$, solid lines) for $St = 0.1$ (orange), $St = 1$ (blue) and $St = 10$ (purple). The spectra are averaged both in space, along the spanwise direction, and time, within the interval $\Delta t^* = 0.003$ centred at time $t^* = 0.0156 \equiv \mathcal{T}_{ripples}^*$. In all cases, spectra are characterized by a peak, indicated with a filled circle, that occurs at slightly different wavenumbers $k_{x,max}$, and is associated with the presence of the ice ripples. Spectra in the inset, corresponding to the $Re_{\tau,0} = 170$ case, exhibit no peak.

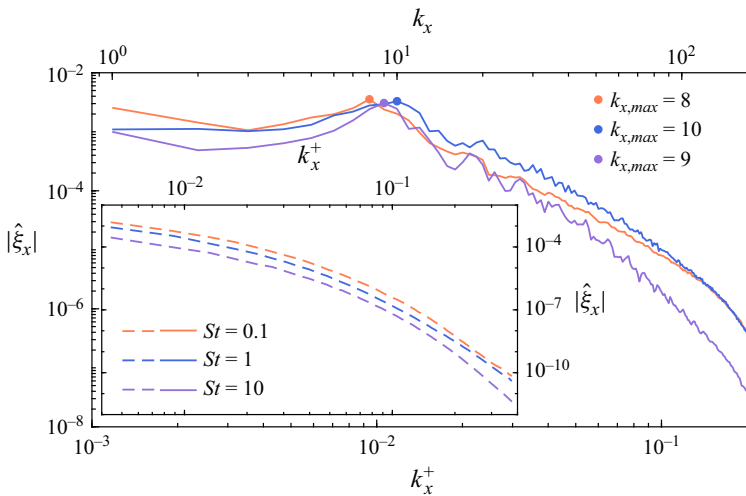


Figure 13. Spanwise spectra of the ice layer thickness, $|\hat{\xi}_x|$, in the supercritical regime ($Re_{\tau,0} = 636$) for $St = 0.1$ (orange), $St = 1$ (blue) and $St = 10$ (purple). All the spectra are averaged along the streamwise direction and in time, over a short time interval $\Delta t^* = 0.003$ centred at time $t^* = 0.0156 \equiv \mathcal{T}_{ripples}^*$. The inset shows the rescaled spectra, $|\hat{\xi}_x^*| = Pe\sqrt{St + Q}|\hat{\xi}_x|$, also for the subcritical regime (dashed lines). All curves overlap, indicating that the (Pe, St) scaling holds regardless of the morphodynamic regime.

4.3. Characterization of ripple dynamics

As discussed in the previous section, the key morphological feature in the supercritical regime is the presence of the ice ripples. In this section, we examine their growth over time, which occurs because the heat flux supplied by the warm water stream is not in phase with the ice layer thickness, ξ . In particular, ice ripples can grow only if the heat flux lags behind ξ by an angle greater than $\pi/2$ (Ashton & Kennedy 1972; Gilpin *et al.* 1980).

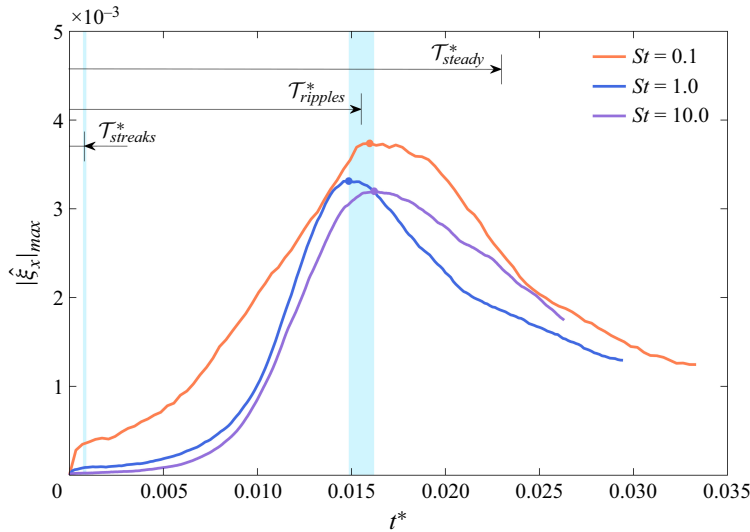


Figure 14. Time evolution of the maximum value, $|\hat{\xi}_x|_{\max}$, of the streamwise spectrum of the ice thickness as a function of the rescaled time, t^* , at varying St . As shown in figure 12, the peak value is obtained at $k_x = 8$ for $St = 0.1$ (orange), at $k_x = 10$ for $St = 1$ (blue) and at $k_x = 9$ for $St = 10$ (purple). Regardless of St , the amplitude grows in the early stages of the simulation, reaching a maximum (marked by a dot) within a relatively narrow range, represented by the larger light blue vertical band. This range does depend on St and is centred at $t^* \approx 0.0156 \equiv \mathcal{T}_{ripples}^*$. Note that $\mathcal{T}_{ripples}^*$ is significantly larger than $\mathcal{T}_{streaks}^*$ while being of the same order of \mathcal{T}_{steady}^* . The final stages of the evolution are characterized by a decay of the amplitude due to the increasing strength of heat conduction within the ice layer, which eventually leads to the steady state.

Physically, this means that the amplitude of the ripples increases only if the heat flux perturbations induced by the wavy interface reach a minimum near the crest and a maximum near the trough.

To quantify the growth of the ice ripples and its dependence on St , in figure 14 we show the time evolution of $|\hat{\xi}_x|_{\max}$, which corresponds to the peak value of the spectra in figure 12 and represents the amplitude of the frequency mode associated with the ice ripples. It is apparent that the qualitative behaviour of $|\hat{\xi}_x|_{\max}$ does not depend on St . The amplitude of the ripples grows in the early stages of the simulations, during the transient dominated by the already-formed turbulence-driven ice streaks. Around time $t^* \approx 0.0085$, namely at approximately one-third of the supercritical, steady-state time \mathcal{T}_{steady}^* , the mode associated with the ice ripples becomes dominant in the streamwise spectra, thus marking the transition to a phase in which the ice morphology is dominated by the ice ripples growth. The ice ripples reach their maximum amplitude around $t^* \approx 0.0160$ for $St = 0.1$, $t^* \approx 0.0149$ for $St = 1$ and $t^* \approx 0.0162$ for $St = 10$, namely within a relatively narrow interval (highlighted in light blue in figure 14) centred at $\mathcal{T}_{ripples}^* \approx 0.0156$. This confirms the large time separation that characterizes the formation of streaks and ripples ($\mathcal{T}_{ripples}^*/\mathcal{T}_{streaks}^* \gg 1$), and suggests that these two processes can be decoupled and modelled separately.

We observe also that $\mathcal{T}_{ripples}^*$ is roughly equal to 2/3 of the steady-state time reported in figure 10, namely $\mathcal{T}_{ripples}^*/\mathcal{T}_{steady}^* \simeq O(1)$: this implies that the morphodynamic evolution of the ice ripples is strongly dependent on the average thickness of the ice layer. This is consistent with the theory formulated by Ashton & Kennedy (1972). According to this theory, the growth rate of the ice ripples depends on two competing effects: the heat

flux supplied by the warm water flow, which increases the amplitude of the ripples, and the diffusive heat flux from the ice layer, which flattens the ripples. The latter is closely related to the average thickness of the ice layer since, as $\langle \xi \rangle$ decreases, the diffusive heat flux through the ice layer increases (in the quasistationary approximation, it is inversely proportional to $\langle \xi \rangle$). At some point, the diffusive heat flux overcomes the effect of the heat flux supplied by the water stream, leading to a reduction of $|\hat{\xi}_x|_{max}$ and explaining the decaying trend observed in figure 10 at times larger than $\mathcal{T}_{ripples}^*$. The decay suggests that ripples would not form if the supercritical simulations were started using the ice layer morphology at equilibrium as initial condition. This shows that the formation of ice ripples is favoured when the ice layer is shrinking. The maximum value of the ice ripples amplitude for $St = 1$ and $St = 10$ is similar, while being larger for $St = 0.1$. This could be due to the fact that the diffusive heat flux through the ice layer does not immediately adjust to changes in the ice morphology but is delayed due to the time scales at which the thermal diffusivity acts. This delay may hamper the capability of heat diffusion within the ice to flatten the interface. Besides this low- St effect, however, the limited variability we observe for the maximum amplitudes is not surprising. It is reasonable to assume that heat flux anomalies at the ice–water interface are mostly influenced by the ice morphology and therefore do not depend on the latent heat.

Figure 14 also shows a nearly exponential growth of $|\hat{\xi}_x|_{max}$ for $St = 1$ and $St = 10$. This is again consistent with the theory by Ashton & Kennedy (1972), which associates the growth of amplitude of the ripples to a time scale that is directly proportional to the thermal diffusivity (namely Pe^{-1}) and inversely proportional to the latent heat (namely St^{-1}). As a result, the growth rate of the ripples at larger St should be similar when evaluated in terms of the rescaled time t^* . We remark here that, in our problem, t^* also depends on the additional sensible heat contribution \mathcal{Q} , defined in § 2.2. This contribution is not accounted for in the theory by Ashton & Kennedy (1972), which is based on the quasistationary approximation for the temperature fields. As discussed in § 2, this condition holds only for very large St , so the effect of \mathcal{Q} must be included for a proper comparison at low St , when such approximation does not hold. For $St = 0.1$, we observe an earlier onset of the growth due to the low latent heat flux, quickly followed by a slower increase compared with the two cases at higher St , limited by the propagation speed of thermal diffusivity.

5. Conclusions

In this paper, we have investigated how the morphology of an ice layer changes over time when subject to the melting induced by a turbulent flow of warm water. The main objective of the study is to examine the different patterns that form at the ice–water interface as melting takes place in connection with the time and length scales that characterize the problem. The time scales, in particular, have been quantified in terms of two dimensionless numbers: the Péclet number and the Stefan number, the latter being the most relevant parameter for the purposes of our analysis because it quantifies the separation between the time scales of heat diffusion and melting. In addition, to fully describe the physical system, we have considered the role of the Reynolds number of the water stream, which governs the separation between the advection and viscous time scales of the system but also influences the features of the ice morphology.

We have first developed a 1-D model based on the solution of a two-phase Stefan problem to estimate the time scale that is required to reach the steady state, namely to melt all the ice that can be melted for a given (imposed) thermal heat flux supplied to the ice by the water. The model relies on the assumption that heat diffusion within the

ice layer is significantly faster than melting. This is indeed what happens in a realistic melting scenario, where the Stefan number is typically very large and the temperature distribution in the ice layer adapts quickly to the modifications of the ice–water interface morphology that are caused by melting. The predictive capability of the model has been assessed successfully by comparing its predictions with the numerical solution of the governing equations of the Stefan problem. Then, the model has been used to estimate the computational cost of a three-dimensional (3-D), time-dependent simulation aiming at reproducing the interface morphodynamics in realistic environmental ice melting processes. By doing so, we have been able to define a range of computational feasibility for the Stefan number, which scales with the magnitude of the latent heat contribution that characterizes melting, but also provide a tool to identify the largest scale separation that is computationally affordable for DNS.

Based on the model estimates, we performed simulations over two orders of magnitude of the Stefan number, up to $St = 10$, and different Reynolds numbers, $Re_{\tau,0}$ for a total of six different cases. The selected Reynolds numbers correspond to two distinct morphodynamic regimes: a subcritical regime, associated with the lower value of $Re_{\tau,0}$, in which the near-wall turbulence of the water stream generates streamwise-oriented streaky structures of ice at the ice–water interface, and a supercritical regime, associated with the higher value of Re , in which ripples emerge and coexist with the much smaller streamwise ice streaks. Our results show that the streamwise ice streaks are only marginally affected by St and the mechanism that leads to their formation is essentially the same in both regimes. The characteristic time scale of streak formation is smaller than the characteristic time required to reach the steady state of the ice melting process, especially in the supercritical regime. However, we have also observed that the ice ripples in this regime undergo complex dynamics that are quantitatively modulated by St : the ripples grow in the early stages of the melting process and later decay once the ice layer becomes thinner due to the competing effects of turbulence-driven convection and heat diffusion within the ice layer. The typical time required to maximize the amplitude of the ripples is found to be comparable to the time required to reach the steady state. We find that the morphological features of the ice–water interface are only weakly influenced by St . Therefore, it is reasonable to infer that the heat distribution is also weakly affected, with the possible exception of the amplitude of the local heat flux perturbations. However, a detailed investigation of how the ice morphodynamics influence the heat transfer rate would require a more comprehensive analysis that is out of scope for the present work.

An important finding of our work is that the most relevant features of the ice–water interface morphology, and not just the average ice thickness, appear to scale consistently with Pe and St . For instance, we have reported that the spectral properties of the streamwise-oriented ice streaks (i.e. their typical size), scale with $Pe^{-1} St^{-0.5}$. We have shown as well that all the relevant time scales of the problem, such as the time required to reach the equilibrium ice layer thickness, the growth rate of the ice ripples and the time at which the ripples attain their maximum amplitude, scale with Pe^{-1} and St^{-1} . A fundamental aspect of these scalings, especially for the low and intermediate values of St considered in our study, is the contribution by the sensible heat, Q , which brings the meltwater generated by the melting of the interface to the same local temperature of the water stream. In our opinion, the scalings that we were able to identify, can help to predict the ice morphodynamics at the very high values of the Péclet and Stefan numbers that characterize real melting processes, which are computationally unfeasible for DNS. For instance, the (Pe, St) scaling could be used to infer the main morphodynamic features from DNS datasets generated at lower values for Pe and St . This might be a crucial step to

include the morphodynamical effects into the large-scale geophysical models for melting ice, therefore helping to improve their accuracy and that of global climate predictions.

Supplementary movies. Supplementary movies are available at <https://doi.org/10.1017/jfm.2025.10615>.

Acknowledgements. We acknowledge the CINECA award under the ISCRA initiative, for the availability of high-performance computing resources and support (Project ID: HP10BHKWVA) and EURO-HPC JU for awarding us access to LUMI-C@LUMI, Finland (Project ID: EHPC-EXT-2022E01-003). The authors acknowledge TU Wien Bibliothek for financial support through its Open Access Funding Programme.

Funding. We gratefully acknowledge financial support from the European Union-NextGenerationEU PNRR M4.C2.1.1 - PRIN 2022, ‘The fluid dynamics of interfaces: mesoscale models for bubbles, droplets, and membranes and their coupling to large scale flows’ 2022R9B2 MW - G53C24000810001, from the European Union-NextGenerationEU PRIN 2022, ‘Next-generation multiscale modelling of dense emulsions for enhanced multiphase flow processes’ 20229WJBPS - E53D23002940006 and the funding from the REACT EU Italian PON 2014-2020 Program, Action IV.5 – Green (DM1062 10/08/2021).

Declaration of interests. The authors report no conflict of interest.

Data availability statement. Data available on request from the authors.

Appendix A. Non-dimensionalization

All the equations of the 1-D model and 3-D simulations, are made non-dimensional using a reference length \tilde{h}_{ref} (that is the height of the channel \tilde{h} for the 3-D simulations), and a reference velocity \tilde{u}_{ref} (that is the shear velocity \tilde{u}_τ for the 3-D simulations), namely

$$(x, y, z) = \frac{(\tilde{x}, \tilde{y}, \tilde{z})}{\tilde{h}_{ref}}, \quad t = \frac{\tilde{u}_{ref}}{\tilde{h}_{ref}} \tilde{t}, \quad \nabla \bullet = \frac{\tilde{\nabla} \bullet}{\tilde{h}_{ref}}, \quad \nabla^2 \bullet = \frac{\tilde{\nabla}^2 \bullet}{\tilde{h}_{ref}^2}. \quad (A1)$$

In the previous, and in the rest of the following derivation, all the quantities marked with the tilde are dimensional, while for their non-dimensional counterpart the tilde is dropped. The momentum equation in the dimensional form reads as

$$\frac{\partial \tilde{\mathbf{u}}}{\partial \tilde{t}} = \tilde{\nu} \tilde{\nabla}^2 \tilde{\mathbf{u}} - \tilde{\mathbf{u}} \cdot \tilde{\nabla} \tilde{\mathbf{u}} - \frac{\tilde{\nabla} \tilde{p}}{\tilde{\rho}} - \frac{\phi^2}{\tilde{\eta}_s} \tilde{\mathbf{u}} \quad (A2)$$

where $\tilde{\rho}$ is the density, $\tilde{\nu}$ the kinematic viscosity and $\tilde{\eta}_s$ the relaxation time for the IBM. The former, in non-dimensional form becomes

$$\frac{\partial \mathbf{u}}{\partial t} = \frac{1}{Re_\tau} \nabla^2 \mathbf{u} - \mathbf{u} \cdot \nabla \mathbf{u} - \nabla p - \frac{\phi^2}{\eta_s} \mathbf{u}, \quad (A3)$$

where

$$\mathbf{u} = \frac{\tilde{\mathbf{u}}}{\tilde{u}_{ref}}, \quad p = \frac{\tilde{p}}{\tilde{\rho} \tilde{u}_{ref}^2}, \quad \eta_s = \frac{\tilde{u}_{ref}}{\tilde{h}_{ref}} \tilde{\eta}_s. \quad (A4)$$

The EN, in the dimensional form reads as

$$\frac{\partial \tilde{\theta}}{\partial \tilde{t}} = \frac{\tilde{\lambda}}{\tilde{\rho} \tilde{c}_p} \tilde{\nabla}^2 \tilde{\theta} - \tilde{\mathbf{u}} \cdot \tilde{\nabla} \tilde{\theta} + \frac{\tilde{\mathcal{L}}}{\tilde{c}_p} \frac{\partial \phi}{\partial \tilde{t}}, \quad (A5)$$

where \tilde{c}_p is the specific heat, $\tilde{\lambda}$ the thermal conductivity and $\tilde{\mathcal{L}}$ the specific latent heat. The former, in non-dimensional form becomes

$$\frac{\partial \theta}{\partial t} = \frac{1}{Pe} \nabla^2 \theta - \mathbf{u} \cdot \nabla \theta + St \frac{\partial \phi}{\partial t} \quad (A6)$$

where temperature is made non-dimensional employing the reference temperature difference of the problem as follows

$$\theta = \frac{\tilde{\theta} - \tilde{\theta}_m}{\Delta\tilde{\theta}}. \quad (\text{A7})$$

The reference temperature, is defined for this problem as the difference between the melting temperature $\tilde{\theta}_m$ and the imposed temperature at the cold wall $\tilde{\theta}_c$, namely $\Delta\tilde{\theta} = (\tilde{\theta}_m - \tilde{\theta}_c)$. The Stefan condition in the dimensional form reads as

$$\tilde{\rho}\mathcal{L}\frac{d\tilde{\xi}}{d\tilde{t}} = \tilde{\lambda} \left. \frac{\partial\tilde{\theta}}{\partial\tilde{x}} \right|_{\tilde{x}=\tilde{\xi}} + \tilde{q}_w, \quad (\text{A8})$$

where \tilde{c}_p is the specific heat, $\tilde{\lambda}$ the thermal conductivity and $\tilde{\mathcal{L}}$ the specific latent heat. The former, in non-dimensional form, becomes

$$Pe\,St\frac{d\xi}{dt} = \left. \frac{\partial\theta}{\partial x} \right|_{x=\xi} + q_w, \quad (\text{A9})$$

where

$$\xi = \frac{\tilde{\xi}}{\tilde{h}_{ref}}, \quad q_w = \frac{\tilde{h}_{ref}}{\tilde{\lambda}\Delta\tilde{\theta}}\tilde{q}_w. \quad (\text{A10})$$

For the phase field, we employed the same AC equation presented by Hester *et al.* (2020), simplified for the single component case,

$$\frac{5}{6}\frac{\tilde{\rho}\tilde{\mathcal{L}}}{\tilde{\lambda}}\frac{\partial\phi}{\partial\tilde{t}} - \tilde{\gamma}\tilde{\nabla}^2\phi = -\frac{1}{\tilde{\epsilon}^2}\phi(1-\phi)[\tilde{\gamma}(1-2\phi) + \tilde{\epsilon}(\tilde{\theta} - \tilde{\theta}_m)], \quad (\text{A11})$$

where the constants $\tilde{\epsilon}$ and $\tilde{\gamma}$ are phase field parameters. By introducing the following quantities

$$\epsilon = \frac{\tilde{\epsilon}}{\tilde{h}}, \quad \mathcal{C} = \frac{\tilde{\epsilon}}{\tilde{\gamma}}\Delta\tilde{\theta}, \quad (\text{A12})$$

the dimensionless AC equation reads as

$$\frac{\partial\phi}{\partial t} = \frac{6}{5\mathcal{C}}\frac{1}{Pe\,St} \left[\nabla^2\phi - \frac{1-\phi}{\epsilon^2}\phi(1-2\phi + \mathcal{C}\theta) \right]. \quad (\text{A13})$$

Appendix B. Analytical solution of the quasistationary Stefan problem

By performing the following change of coordinates

$$\eta = z/\xi(t), \quad \psi = \int_0^t \xi^{-2}(\tau)d\tau, \quad (\text{B1})$$

the system (2.1) can be rewritten as

$$\begin{cases} Pe\,St\frac{d\xi}{d\psi} = \xi \left. \frac{\partial\theta}{\partial\eta} \right|_{\eta=1} + \xi^2 q_w, \\ \frac{\partial\theta}{\partial\psi} = \frac{1}{Pe} \frac{\partial^2\theta}{\partial\eta^2} + \frac{\partial\theta}{\partial\eta} \frac{d\xi}{dt} \xi\eta, \end{cases} \quad (\text{B2})$$

with the assumption that $\xi \neq 0$ for $t > 0$. The standard Fourier equation is recovered from the second equation of (B2) if

$$\frac{1}{Pe} \frac{\partial^2 \theta}{\partial \eta^2} \gg \frac{\partial \theta}{\partial \eta} \frac{d\xi}{dt} \xi \eta, \quad (\text{B3})$$

which can be expressed in terms of τ_D and τ_M ,

$$\frac{\Delta \theta}{\tau_D} \xi^2 \gg \frac{\Delta \theta}{\tau_M} \xi^2. \quad (\text{B4})$$

Therefore, if $\tau_M \gg \tau_D$, then the temperature field does not depend on ψ , being the initial condition for θ already a steady solution for the standard Fourier equation,

$$\theta(\eta, \psi) = \theta_c (1 - \eta). \quad (\text{B5})$$

This allows to rewrite the first equation of (B2) as

$$Pe St \frac{d\xi}{d\psi} = \xi \left. \frac{\partial \theta}{\partial \eta} \right|_{\eta=1} + \xi^2 q_w = -\theta_c \xi + q_w \xi^2. \quad (\text{B6})$$

When $q_w \neq 0$ (the case $q_w = 0$ is trivial), (B6) can be integrated analytically to obtain

$$\ln \left| \frac{\xi}{\xi - \theta_c/q_w} \right| = -\frac{\theta_c}{Pe St} \psi + c_1, \quad (\text{B7})$$

where c_1 is an integration constant. The interface thickness can then be expressed using the first equation of the system (2.9),

$$\xi(\psi) = \frac{\theta_c}{q_w} \frac{S - 1}{S}, \quad (\text{B8})$$

with

$$S = \begin{cases} 1 - \exp \left[\frac{\theta_c}{Pe St} \psi + c_1 \right] & \text{if } \xi - \theta_c/q_w > 0, \\ 1 + \exp \left[\frac{\theta_c}{Pe St} \psi + c_1 \right] & \text{if } \xi - \theta_c/q_w < 0. \end{cases} \quad (\text{B9})$$

By definition, $\psi = 0$ for $t = 0$ and, therefore, the value of the constant c_1 can be set in order to satisfy the initial condition $\xi(t = 0) = \xi_0$. With this value of c_1 the definition of S , regardless of the sign of $\xi - \theta_c/q_w$, becomes

$$S = 1 - \frac{\xi_0}{\xi_0 - \theta_c/q_w} \exp \left[\frac{\theta_c}{Pe St} \psi \right]. \quad (\text{B10})$$

Note that, if $\xi = \xi_{eq} = \theta_c/q_w$, then the interface is at equilibrium – (B6) shows that ξ does not evolve in time – and the rescaling procedure is not valid anymore. It is possible to derive the second equation of the system (2.9) by using the definitions (B1),

$$dt = \xi^2(\psi) d\psi = \xi^2(\psi) \frac{d\psi}{d\xi} d\xi = \frac{\theta_c^2}{q_w^2} \frac{(S - 1)^2}{S^2} \frac{Pe St}{\theta_c} \frac{1}{S - 1} d\xi = \frac{\theta_c Pe St}{q_w^2} \frac{S - 1}{S^2} d\xi. \quad (\text{B11})$$

This equation can be integrated analytically as

$$\frac{\theta_c}{Pe St} t = \frac{1}{S} + \ln S + c_2, \quad (\text{B12})$$

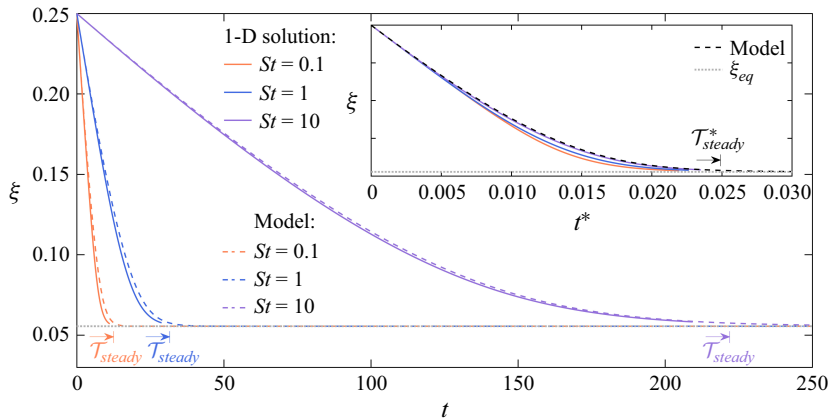


Figure 15. Time evolution of the ice thickness, ξ . The solid lines show the numerical 1-D solution of problem (B2) for $St = 0.1$ (orange), $St = 1$ (blue) and $St = 10$ (purple), respectively. The model predictions are shown by the dashed lines (same colour code). For each value of St , the steady-state time T_{steady} – computed using (2.14) – is also shown. In particular, T_{steady} corresponds to the time at which 99 % of the ice layer has melted before reaching the steady state thickness, $\xi = \xi_{eq}$ (grey dotted line). The inset shows the ice thickness evolution against the rescaled time t^* , as derived from the analytical model. Using this rescaling, the model predictions (represented by the black dashed line) as well as the rescaled steady-state time, T^*_{steady} , become independent of St .

in which c_2 is a further constant of integration. Imposing $\psi = 0$ for $t = 0$ leads to $c_2 = -1/S_0 - \ln S_0$, where $S_0 = S(t = 0)$ and its expression is reported in the system (2.9). With this substitution, (B12) becomes the second equation of the system (2.9).

B.1. Model assessment

To test the validity of the model, its results are compared with the numerical solution of the 1-D problem (B2), coupled with the condition (2.12). The simulation parameters are $\xi_0 = 0.25$, $Pe = 848.4$, $\theta_c = -1$, $q_w = -18$ and $\mathcal{Q} = 0.5$. Here, we analyse the results for three different Stefan numbers: $St = 0.1$, $St = 1$ and $St = 10$. Note that these parameters are similar to those used to perform the 3-D simulations that will be discussed in the next sections. The numerical solution for the system (B2) is computed using a second-order finite difference discretization scheme for the modified Fourier equation: a central scheme is employed for the discretization of the second derivative, while the first derivative of the nonlinear term is computed using an upwind discretization (with respect to the velocity of the moving front). A first-order scheme is used to compute the temperature derivative at the moving boundary, which is needed for the Stefan law. An explicit Euler discretization is used for time stepping.

Results are shown in figure 15, where the time evolution of the ice thickness, $\xi(t)$, is plotted for the three different St analysed. The model (dashed lines) captures very well the dynamics of the moving interface resulting from the 1-D simulations (solid lines) for each value of St . The figure shows also how the time T_{steady} required to reach the steady state condition (computed from (2.14)) is strongly affected by St . In the inset of figure 15, the interface position is plotted as a function of the rescaled time, t^* . According to the model, the predicted ice front position (black dashed line) should become independent of St when t^* is used instead of t . This is indeed what we observe in the plot, even if there is a small discrepancy between the model prediction and the 1-D simulations before the steady state is reached. However, as can also be inferred from the condition (2.8), when the interface thickness approaches the equilibrium value ξ_{eq} , the error tends to vanish. At equilibrium,

$\xi = \theta_c/q_w$ – see (B6) of the manuscript – and the right-hand side of (2.8) becomes zero. As a result, the model is able to capture fairly well the overall dynamics even at low St . Note that the rescaled steady-state time, $\mathcal{T}_{steady}^* \approx 0.025$, is also independent of St .

We remark here that other models, similar to the one presented here, have been reported in the literature (Landau 1950; Murray & Landis 1959; Lunardini 1991; Kurylyk *et al.* 2014), but with different boundary conditions. In addition, sophisticated models to estimate melting in the presence of buoyancy effects and/or accounting for the actual ice morphology have been recently developed (Favier *et al.* 2019; Coustou *et al.* 2021). However, these models require numerical integration and additional input parameters for the morphology, which can only be known through costly simulations. The model we propose neglects morphological effects, but provides an analytical solution that allows to estimate *a priori* (namely before performing the simulation) and very easily the time required to reach the equilibrium condition. This information is crucial to determine beforehand the computational feasibility of a simulation. Consider, for instance, a DNS of an ice layer melted by a turbulent flow of water at shear Reynolds number $Re_\tau \approx \mathcal{O}(10^3)$. Typical water temperatures that can be found in ice-shelf melting are of the order of 1°C , which, considering the thermophysical properties of ice and water, yields $St \approx \mathcal{O}(10^2)$. Such values of Re_τ and St would require a computational cost of around 1.6×10^5 GPU hours on a modern petascale Tier-0 supercomputer, corresponding roughly to 2.25 years of run time. In addition, considering that the typical value of the shear velocity beneath ice shelves is $\tilde{u}_\tau \approx 0.01 \text{ m s}^{-1}$, it can be estimated that only an ice layer 1.7 cm thick would melt during the simulation. These are clearly prohibitive costs, which can be avoided only if simulations at low St , e.g. $St \approx \mathcal{O}(10)$ or lower, can be exploited to infer the actual morphological features of the ice layer at high St , e.g. $St \approx \mathcal{O}(10)$ or higher. Our model could, in principle, be extended to a Rayleigh–Bénard configuration, as in the case of Favier *et al.* (2019). However, unlike the model proposed by Favier *et al.* (2019), we do not assume that the ice is isothermal and fixed at the melting temperature. Instead, we account for the heat conduction that occurs within the ice layer, which becomes relevant when the temperature at the top of the ice layer is maintained below the freezing point. If the heat flux q_b , supplied to the water layer, is constant – as is the case when the Nusselt number scales with the Rayleigh number as $Nu \propto Ra^{1/3}$ (Grossmann & Lohse 2000; Favier *et al.* 2019) – then the analytical solution remains valid in the Rayleigh–Bénard configuration, provided an appropriate value of q_b is used.

REFERENCES

- ALLEY, K.E., SCAMBOS, T.A., SIEGFRIED, M.R. & FRICKER, H.A. 2016 Impacts of warm water on Antarctic ice shelf stability through basal channel formation. *Nat. Geosci.* **9** (4), 290–293.
- ALLEY, R.B., CLARK, P.U., HUYBRECHTS, P. & JOUGHIN, I. 2005 Ice-sheet and sea-level changes. *Science* **310** (5747), 456–460.
- ASHTON, G.D. & KENNEDY, J.F. 1972 Ripples on underside of river ice covers. *J. Hydraul. Div.* **98** (9), 1603–1624.
- BINTANJA, R., REIJMER, C.H. & HULSCHER, S.J.M.H. 2001 Detailed observations of the rippled surface of Antarctic blue-ice areas. *J. Glaciol.* **47** (158), 387–396.
- BUSHUK, M., HOLLAND, D.M., STANTON, T.P., STERN, A. & GRAY, C. 2019 Ice scallops: a laboratory investigation of the ice–water interface. *J. Fluid Mech.* **873**, 942–976.
- CAMPORALE, C. & RIDOLFI, L. 2012 Ice ripple formation at large Reynolds numbers. *J. Fluid Mech.* **694**, 225–251.
- CANUTO, C., HUSSAINI, M.Y., QUARTERONI, A. & ZANG, T.A. 2007 *Spectral Methods: Fundamentals in Single Domains*. Springer Science & Business Media.
- CENEDESE, C. & STRANEO, F. 2023 Icebergs melting. *Annu. Rev. Fluid Mech.* **55**, 377–402.
- CHAIGNE, M., CARPY, S., MASSÉ, M., DERR, J., COURRECH DU PONT, S. & BERHANU, M. 2023 Emergence of tip singularities in dissolution patterns. *Proc. Natl Acad. Sci. USA* **120** (48), e2309379120.

- CHEDEVERGNE, F., STUCK, M., OLAZABAL-LOUMÉ, M. & COUZI, J. 2023 About the role of the Hanratty correction in the linear response of a turbulent flow bounded by a wavy wall. *J. Fluid Mech.* **967**, A39.
- CLARK, P.U., ALLEY, R.B. & POLLARD, D. 1999 Northern Hemisphere ice-sheet influences on global climate change. *Science* **286** (5442), 1104–1111.
- CLAUDIN, P., DURÁN, O. & ANDREOTTI, B. 2017 Dissolution instability and roughening transition. *J. Fluid Mech.* **832**, R2.
- COUSTON, L.A. 2021 Turbulent convection in subglacial lakes. *J. Fluid Mech.* **915**, A31.
- COUSTON, L.A., HESTER, E., FAVIER, B., TAYLOR, J.R., HOLLAND, P.R. & JENKINS, A. 2021 Topography generation by melting and freezing in a turbulent shear flow. *J. Fluid Mech.* **911**, A44.
- CURL, R.L. 1974 Deducing flow velocity in cave conduits from scallops. *Bull. Natl Speleol. Soc.* **36**, 1–5.
- DAVIS, P.E.D. & NICHOLLS, K.W. 2019 Turbulence observations beneath Larsen C ice shelf, Antarctica. *J. Geophys. Res.: Oceans* **124** (8), 5529–5550.
- DHAS, D.J., ROY, A. & TOPPALADODDI, S. 2023 Penetrative and Marangoni convection in a fluid film over a phase boundary. *J. Fluid Mech.* **977**, A34.
- DINNIMAN, M.S., ASAY-DAVIS, X.S., GALTON-FENZI, B.K., HOLLAND, P.R., JENKINS, A. & TIMMERMANN, R. 2016 Modeling ice shelf/ocean interaction in Antarctica: a review. *Oceanography* **29** (4), 144–153.
- DU, Y., CALZAVARINI, E. & SUN, C. 2024 The physics of freezing and melting in the presence of flows. *Nat. Rev. Phys.* **6**, 676–690.
- DU, Y., WANG, Z., JIANG, L., CALZAVARINI, E. & SUN, C. 2023 Sea water freezing modes in a natural convection system. *J. Fluid Mech.* **960**, A35.
- DURAN VINENT, O., ANDREOTTI, B., CLAUDIN, P. & WINTER, C. 2019 A unified model of ripples and dunes in water and planetary environments. *Nat. Geosci.* **12** (5), 345–350.
- EZAT, M.M., FAHL, K. & RASMUSSEN, T.L. 2024 Arctic freshwater outflow suppressed Nordic seas overturning and oceanic heat transport during the last interglacial. *Nat. Commun.* **15** (1), 8998.
- FANG, W.P., WU, J.Z., HUANG, Z.L., WANG, B.F., ZHOU, Q. & CHONG, K.L. 2024 Vibration-induced morphological evolution of a melting solid under microgravity. *J. Fluid Mech.* **1001**, A43.
- FAVIER, B., PURSEED, J. & DUCHEMIN, L. 2019 Rayleigh–Bénard convection with a melting boundary. *J. Fluid Mech.* **858**, 437–473.
- FELTHAM, D.L., WORSTER, M.G. & WETTLAUER, J.S. 2002 The influence of ocean flow on newly forming sea ice. *J. Geophys. Res.: Oceans* **107** (C2), 1–1.
- FITZMAURICE, A., STRANEO, F., CENEDESE, C. & ANDRES, M. 2016 Effect of a sheared flow on iceberg motion and melting. *Geophys. Res. Lett.* **43** (24), 12–520.
- GASTINE, T. & FAVIER, B. 2024 Rotating convection with a melting boundary: an application to the icy moons. *Icarus* **429**, 116441.
- GILPIN, R.R., HIRATA, T. & CHENG, K.C. 1980 Wave formation and heat transfer at an ice-water interface in the presence of a turbulent flow. *J. Fluid Mech.* **99** (3), 619–640.
- GOLDBERG, D.N., GOURMELEN, N., KIMURA, S., MILLAN, R. & SNOW, K. 2019 How accurately should we model ice shelf melt rates? *Geophys. Res. Lett.* **46** (1), 189–199.
- GOLLEDGE, N.R., KELLER, E.D., GOMEZ, N., NAUGHTEN, K.A., BERNALDES, J., TRUSEL, L.D. & EDWARDS, T.L. 2019 Global environmental consequences of twenty-first-century ice-sheet melt. *Nature* **566** (7742), 65–72.
- GROSSMANN, S. & LOHSE, D. 2000 Scaling in thermal convection: a unifying theory. *J. Fluid Mech.* **407**, 27–56.
- HANRATTY, T.J. 1981 Stability of surfaces that are dissolving or being formed by convective diffusion. *Annu. Rev. Fluid Mech.* **13** (1), 231–252.
- HESTER, E.W., MCCONNOCHIE, C.D., CENEDESE, C., COUSTON, L.A. & VASIL, G. 2021 Aspect ratio affects iceberg melting. *Phys. Rev. Fluids* **6** (2), 023802.
- HESTER, E.W., COUSTON, L.A., FAVIER, B., BURNS, K.J. & VASIL, G.M. 2020 Improved phase-field models of melting and dissolution in multi-component flows. *Proc. R. Soc. Lond. A: Math. Phys. Engng Sci.* **476** (2242), 20200508.
- HEWITT, I.J. 2020 Subglacial plumes. *Annu. Rev. Fluid Mech.* **52** (1), 145–169.
- HIRANO, D., *et al.* 2023 On-shelf circulation of warm water toward the Totten ice shelf in East Antarctica. *Nat. Commun.* **14** (1), 4955.
- HOBSON, B.W., SHERMAN, A.D. & MCGILL, P.R. 2011 Imaging and sampling beneath free-drifting icebergs with a remotely operated vehicle. *Deep Sea Res. II: Top. Stud. Oceanogr.* **58** (11–12), 1311–1317.
- HSU, K.S., LOCHER, F.A. & KENNEDY, J.F. 1979 Forced-convection heat transfer from irregular melting wavy boundaries. *J. Heat Transfer* **101** (4), 598–602.
- JIA, P., ANDREOTTI, B. & CLAUDIN, P. 2023 Hydrodynamic roughness induced by a multiscale topography. *J. Fluid Mech.* **974**, A16.

- JOUGHIN, I. & ALLEY, R.B. 2011 Stability of the West Antarctic ice sheet in a warming world. *Nat. Geosci.* **4**, 506–513.
- JOURDAIN, N.C., ASAY-DAVIS, X., HATTERMANN, T., STRANEO, F., SEROUSSI, H., LITTLE, C.M. & NOWICKI, S. 2020 A protocol for calculating basal melt rates in the ISMIP6 Antarctic ice sheet projections. *Cryosphere* **14** (8), 3111–3134.
- KHOSRONEJAD, A. & SOTIROPOULOS, F. 2017 On the genesis and evolution of barchan dunes: morphodynamics. *J. Fluid Mech.* **815**, 117–148.
- KURYLYK, B.L., MCKENZIE, J.M., MACQUARRIE, K.T.B. & VOSS, C.I. 2014 Analytical solutions for benchmarking cold regions subsurface water flow and energy transport models: one-dimensional soil thaw with conduction and advection. *Adv. Water Resour.* **70**, 172–184.
- LANDAU, H.G. 1950 Heat conduction in a melting solid. *Q. Appl. Maths* **8** (1), 81–94.
- LIN, T.C. & QUN, P. 1987 On the formation of regmaglypts on meteorites. *Fluid Dyn. Res.* **1** (3–4), 191–199.
- LUCIEER, V., NAU, A.W., FORREST, A.L. & HAWES, I. 2016 Fine-scale sea ice structure characterized using underwater acoustic methods. *Remote Sens.* **8** (10), 821.
- LUNARDINI, V.J. 1991 *Heat Transfer with Freezing and Thawing*. Elsevier.
- MAGNANI, M., MUSACCHIO, S., PROVENZALE, A. & BOFFETTA, G. 2024 Convection in the active layer speeds up permafrost thaw in coarse-grained soils. *Phys. Rev. Fluids* **9** (8), L081501.
- MARCHIOLI, C. & SOLDATI, A. 2002 Mechanisms for particle transfer and segregation in a turbulent boundary layer. *J. Fluid Mech.* **468**, 283–315.
- MURRAY, W.D. & LANDIS, F. 1959 Numerical and machine solutions of transient heat-conduction problems involving melting or freezing: part I – method of analysis and sample solutions. *J. Heat Transfer* **81** (2), 106–112.
- PATMORE, R.D., HOLLAND, P.R., VREUGDENHIL, C.A., JENKINS, A. & TAYLOR, J.R. 2023 Turbulence in the ice shelf–ocean boundary current and its sensitivity to model resolution. *J. Phys. Oceanogr.* **53** (2), 613–633.
- PERISSUTTI, D., MARCHIOLI, C. & SOLDATI, A. 2024 Morphodynamics of melting ice over turbulent warm water streams. *Intl J. Multiphase Flow* **181**, 105007.
- PRITCHARD, H.D., LIGTENBERG, S.R.M., FRICKER, H.A., VAUGHAN, D.G., VAN DEN BROEKE, M.R. & PADMAN, L. 2012 Antarctic ice-sheet loss driven by basal melting of ice shelves. *Nature* **484** (7395), 502–505.
- RABBANIPOUR ESFAHANI, B., HIRATA, S.C., BERTI, S. & CALZAVARINI, E. 2018 Basal melting driven by turbulent thermal convection. *Phys. Rev. Fluids* **3** (5), 053501.
- RAMUDU, E., HIRSH, B.H., OLSON, P. & GNANADESIKAN, A. 2016 Turbulent heat exchange between water and ice at an evolving ice–water interface. *J. Fluid Mech.* **798**, 572–597.
- RIGNOT, E., JACOBS, S., MOUGINOT, J. & SCHEUCHL, B. 2013 Ice-shelf melting around Antarctica. *Science* **341** (6143), 266–270.
- ROCCON, A. 2024 A GPU-ready pseudo-spectral method for direct numerical simulations of multiphase turbulence. *Procedia Comput. Sci.* **240**, 17–30.
- ROCCON, A., SOLIGO, G. & SOLDATI, A. 2025 Flow36: a spectral solver for phase-field based multiphase turbulence simulations on heterogeneous computing architectures. *Comput. Phys. Commun.* **313**, 109640.
- ROCCON, A., ZONTA, F. & SOLDATI, A. 2023 Phase-field modeling of complex interface dynamics in drop-laden turbulence. *Phys. Rev. Fluids* **8** (9), 090501.
- SOLIGO, G., ROCCON, A. & SOLDATI, A. 2021 Turbulent flows with drops and bubbles: what numerical simulations can tell us – Freeman scholar lecture. *J. Fluids Engng* **143** (8), 080801.
- THOMAS, R.M. 1979 Size of scallops and ripples formed by flowing water. *Nature* **277** (5694), 281–283.
- THORSNESS, C.B., MORRISROE, P.E. & HANRATTY, T.J. 1978 A comparison of linear theory with measurements of the variation of shear stress along a solid wave. *Chem. Engng Sci.* **33** (5), 579–592.
- TOPPALADODDI, S. & WELLS, A.J. 2025 Stochastic model for the turbulent ocean heat flux under Arctic sea ice. *Phys. Rev. E* **111**, 025101.
- TOPPALADODDI, S. & WETTLAUER, J.S. 2019 The combined effects of shear and buoyancy on phase boundary stability. *J. Fluid Mech.* **868**, 648–665.
- WANG, Z., CALZAVARINI, E. & SUN, C. 2021a Equilibrium states of the ice-water front in a differentially heated rectangular cell. *Europhys. Lett.* **135** (5), 54001.
- WANG, Z., CALZAVARINI, E., SUN, C. & TOSCHI, F. 2021b How the growth of ice depends on the fluid dynamics underneath. *Proc. Natl Acad Sci. USA* **118** (10), e2012870118.
- WANG, Z., JIANG, L., DU, Y., SUN, C. & CALZAVARINI, E. 2021c Ice front shaping by upward convective current. *Phys. Rev. Fluids* **6** (9), L091501.
- WASHAM, P., *et al.* 2023 Direct observations of melting, freezing, and ocean circulation in an ice shelf basal crevasse. *Sci. Adv.* **9** (43), eadi7638.

- WETTTLAUER, J.S. 1991 Heat flux at the ice-ocean interface. *J. Geophys. Res.: Oceans* **96** (C4), 7215–7236.
- YANG, R., CHONG, K.L., LIU, H.R., VERZICCO, R. & LOHSE, D. 2022 Abrupt transition from slow to fast melting of ice. *Phys. Rev. Fluids* **7** (8), 083503.
- YANG, R., HOWLAND, C.J., LIU, H.R., VERZICCO, R. & LOHSE, D. 2023*a* Bistability in radiatively heated melt ponds. *Phys. Rev. Lett.* **131** (23), 234002.
- YANG, R., HOWLAND, C.J., LIU, H.R., VERZICCO, R. & LOHSE, D. 2023*b* Morphology evolution of a melting solid layer above its melt heated from below. *J. Fluid Mech.* **956**, A23.
- YANG, R., HOWLAND, C.J., LIU, H.R., VERZICCO, R. & LOHSE, D. 2024 Shape effect on solid melting in flowing liquid. *J. Fluid Mech.* **980**, R1.
- YIZHAQ, H., *et al.* 2024 Coevolving aerodynamic and impact ripples on earth. *Nat. Geosci.* **17** (1), 66–72.
- YOSHIHIRO, N., *et al.* 2019 Pathways of ocean heat towards Pine Island and Thwaites grounding lines. *Sci. Rep.* **9**, 16649.
- ZONTA, F., SICHANI, P.H. & SOLDATI, A. 2022 Interaction between thermal stratification and turbulence in channel flow. *J. Fluid Mech.* **945**, A3.
- ZONTA, F. & SOLDATI, A. 2018 Stably stratified wall-bounded turbulence. *Appl. Mech. Rev.* **70** (4), 040801.